

Article

# Role of Semiconductive Property on Selective Cementation Mechanism of Iron Oxides to Gold in Galvanic Interaction with Zero-Valent Aluminum from Gold–Copper Ammoniacal Thiosulfate Solutions

Joshua Zoleta <sup>1,2,\*</sup>, Kosei Aikawa <sup>3,\*</sup>, Nako Okada <sup>1</sup>, Ilhwan Park <sup>3</sup>, Mayumi Ito <sup>3</sup>, Yogarajah Elakneswaran <sup>3</sup> and Naoki Hiroyoshi <sup>3</sup>

<sup>1</sup> Division of Sustainable Resources Engineering, Graduate School of Engineering, Hokkaido University, Sapporo 060-8628, Japan

<sup>2</sup> Department of Materials and Resources Engineering, College of Engineering and Technology, Mindanao State University-Iligan Institute of Technology, Iligan City 9200, Philippines

<sup>3</sup> Division of Sustainable Resources Engineering, Faculty of Engineering, Hokkaido University, Sapporo 060-8628, Japan; i-park@eng.hokudai.ac.jp (I.P.); hiroyosi@eng.hokudai.ac.jp (N.H.)

\* Correspondence: joshua.zoleta@g.msuiit.edu.ph (J.Z.); k-aikawa@eng.hokudai.ac.jp (K.A.); Tel.: +63-9171580601 (J.Z.)

**Abstract:** Iron oxides (hematite, Fe<sub>2</sub>O<sub>3</sub>, and magnetite, Fe<sub>3</sub>O<sub>4</sub>), previously used as electron mediators in the galvanic system with zero-valent aluminum (ZVAL), have been shown to recover Au upon cementation in Au–Cu ammoniacal thiosulfate media selectively, and this warrants further investigation. This research is focused on investigating the role of the semiconductive properties of metal oxides by performing a cementation experiment by mixing 0.15 g of electron mediators (Fe<sub>3</sub>O<sub>4</sub>, Fe<sub>2</sub>O<sub>3</sub>, TiO<sub>2</sub> (anatase and rutile)) and 0.15 g of zero-valent aluminum powder as an electron donor in various electrochemical experiments. The results revealed that upon the cementation experiment, synthetic Fe<sub>2</sub>O<sub>3</sub> and Fe<sub>3</sub>O<sub>4</sub> were consistently able to selectively recover Au at around 90% and Cu at around 20%. Compared to activated carbon (AC), TiO<sub>2</sub>, in anatase and rutile forms, obtained selective recovery of gold, but the recovery was utterly insignificant compared to that of iron oxides, obtaining an average of 93% Au and 63% Cu recovery. The electrochemical and surface analysis supports the results obtained upon the cementation process, where TiO<sub>2</sub>, upon cyclic voltammetry (CV), obtained two reduction peaks centered at –1.0 V and –0.5 V assigned to reducing Au and Cu ions, respectively. Furthermore, various electrochemical impedance spectroscopic analyses revealed that the flat band potential obtained in the Mott–Schottky plot is around –1.0 V and –0.2 V for iron oxides and titanium oxides, respectively, suggesting that the electrons travel from semiconductor interface to electrolyte interface, and electrons are accessible only to Au ions in the electrolyte interface (reduction band edge around –1.0 V). The determination of this selective cementation mechanism is one of a kind. It has been proposed that the semiconductive properties of Fe<sub>2</sub>O<sub>3</sub>, Fe<sub>3</sub>O<sub>4</sub>, and, by configuring their relative energy band diagram, the travel of electrons from the iron oxide–electrolyte interface facilitate the selective cementation towards Au(S<sub>2</sub>O<sub>3</sub>)<sub>2</sub><sup>3+</sup> ions in gold–copper ammoniacal thiosulfate solutions.

**Keywords:** ammoniacal thiosulfate leaching; reductive precipitation; galvanic interactions; cyclic voltammetry; chronoamperometry; iron oxides



**Citation:** Zoleta, J.; Aikawa, K.; Okada, N.; Park, I.; Ito, M.; Elakneswaran, Y.; Hiroyoshi, N. Role of Semiconductive Property on Selective Cementation Mechanism of Iron Oxides to Gold in Galvanic Interaction with Zero-Valent Aluminum from Gold–Copper Ammoniacal Thiosulfate Solutions. *Metals* **2024**, *14*, 550. <https://doi.org/10.3390/met14050550>

Academic Editor: Antoni Roca

Received: 5 March 2024

Revised: 2 May 2024

Accepted: 6 May 2024

Published: 7 May 2024



**Copyright:** © 2024 by the authors. Licensee MDPI, Basel, Switzerland. This article is an open access article distributed under the terms and conditions of the Creative Commons Attribution (CC BY) license (<https://creativecommons.org/licenses/by/4.0/>).

## 1. Introduction

Gold and the lucrative value it bears have caused and continue to cause an increase in demand, which spiked its price up to USD 2000 per ounce, as this precious and novel metal has been used in several applications, such as the use of gold in official coins, in electronic devices, and in other applications, such as the use of gold in medical applications [1–3].

These demands have become a significant research interest for sustainability, knowing that the natural gold ore reserves are depleting and are finite resources; as such, finding alternative resources is a critical issue to be addressed [2]. One potential gold resource is the tailings deposits operated by mining companies dealing with refractory gold pyritic ores. These mining companies have 60–70% overall recovery, and thus, the refractory gold encapsulated in the sulfur matrix of pyrite is a potential resource for gold production [4]. Researchers have been dealing with how this type of ore can be re-exploited. This natural reserve is difficult to refine, as pyrite has a complicated mineralogy. Conventionally, a two-step process has been employed to recover gold from this type of ore successfully. The pyrometallurgical process is conventionally employed to alter pyrite's surface properties to expose the gold on its surface via sulfur oxidation in the oxidation roasting process. The roasted pyrite is now susceptible to chemical dissolution via cyanide leaching [5,6].

On the other hand, many countries have banned this toxic chemical, as this lixiviant has caused and continues to cause detrimental effects to humans and the environment. Much research has been driven to find alternatives, such as investigating halide groups and thiourea, but these chemicals have proven highly corrosive [7–14]. One of the potential candidates is the use of thiosulfate in the gold leaching process. However, it is not currently in use because of its low recovery in pregnant solution; its higher selectivity and leaching rate for gold warrants it being investigated concerning recovery techniques. To address this issue, previous research has proven the possibility of increasing gold recovery via galvanic interaction with zero-valent aluminum, which accounts for up to 99.99% of gold recovery via reductive deposition [1,15].

Previous research has been employed to investigate the feasibility of iron oxides (the main product of roasting pyrite) as electron mediators in galvanic interaction with zero-valent aluminum in gold–copper ammoniacal thiosulfate media to resolve the issue of refractory gold pyritic ores [1]. Also, the previous study reported that iron oxide can be used as an electron mediator and can cement gold up to 90% on its surface [1]. Also, the difference between activated carbon and iron oxide has been highlighted and is the main interest of this study; activated carbon was able to recover both gold and copper at 99.99%, while the use of iron oxides was able to recover gold and copper around 86–90% and 15–21%, respectively. Thus, using iron oxides as electron mediators has selectively cemented gold in a copper ammoniacal thiosulfate medium [1]. The previous findings are advantageous because the copper in a barren solution with ammoniacal thiosulfate can be re-used for gold dissolution as copper ions are the main component in catalyzing gold dissolution. Considering the semiconductive properties of hematite and magnetite, this research is governed by investigating the primary mechanism of selective cementation in the iron oxide–electrolyte interface by conducting in-depth electrochemical impedance spectroscopic analyses of various semiconductive materials.

## 2. Materials and Methods

### 2.1. Materials

All materials with 99.99% purity used in this study were purchased at Wako Pure Chemical Industries, Ltd., Osaka, Japan, where zero-valent aluminum, ZVAI (CAS No.: 012-19172, around 45  $\mu\text{m}$  in diameter) was used as the electron donor. Activated carbon (CAS No.: 031-02135), having about 800–1500  $\text{m}^2/\text{g}$  of specific surface area; hematite,  $\text{Fe}_2\text{O}_3$  (CAS No.: 096-02821); magnetite,  $\text{Fe}_3\text{O}_4$  (CAS No.: 093-01035); anatase,  $\text{TiO}_2$  (CAS No.: 1317-70-0); and rutile,  $\text{TiO}_2$  (CAS No.: 1317-80-2), were used as electron mediators to recover Au ions from ammonium thiosulfate solutions via galvanic interactions. Table 1 summarizes the sample transmittal used in this study.

**Table 1.** Sample transmittal summary.

Single System		Binary System	
Sample Name	Sample ID	Sample Name	Sample ID.
Zero-Valent Aluminum	Al	Activated Carbon/Zero-Valent Aluminum	AC/Al
Activated Carbon	AC	Synthetic Magnetite/Zero-Valent Aluminum	Mag/Al
Synthetic Magnetite	Mag	Synthetic Hematite/Zero-Valent Aluminum	Hem/Al
Synthetic Hematite	Hem	Synthetic TiO <sub>2</sub> (Anatase)/Zero-Valent Aluminum	Anatase/Al
Synthetic TiO <sub>2</sub> (Anatase)	Anatase	Synthetic TiO <sub>2</sub> (Rutile)/Zero-Valent Aluminum	Rutile/Al
Synthetic TiO <sub>2</sub> (Rutile)	Rutile		

## 2.2. Recovery of Gold Ions from Ammoniacal Thiosulfate Solutions

The preparation of Au–Cu ammoniacal thiosulfate solutions was derived from previous research [1], where 0.01 g of Au powder was leached (99.999%, CAS No.: 937902 Wako Pure Chemical Industries, Ltd., Osaka, Japan) in 100 mL of copper ammoniacal thiosulfate solution (containing 1 M Na<sub>2</sub>S<sub>2</sub>O<sub>3</sub>·5H<sub>2</sub>O (CAS No.: 197-03585), 0.5 M NH<sub>3</sub> (CAS No.: 016-03146), 0.25 M (NH<sub>4</sub>)<sub>2</sub>SO<sub>4</sub> (CAS No.: 016-03445), and 10 mM CuSO<sub>4</sub> (CAS No.: 034-04445) from Wako Pure Chemical Industries, Ltd., Osaka, Japan. The solutions were maintained at pH 9–10 using a 300 mL Erlenmeyer flask shaken in a thermostatic water bath shaker at 30 °C for 24 h with a constant shaking amplitude and frequency of 40 mm and 600 min<sup>−1</sup>, respectively.

Furthermore, to evaluate the recovery of dissolved Au, 0.15 g of ZVAL and/or 0.15 g of activated carbon, 0.15 g ZVAL and/or 0.15 g hematite (Fe<sub>2</sub>O<sub>3</sub>), 0.15 g ZVAL and/or 0.15 g magnetite (Fe<sub>3</sub>O<sub>4</sub>), 0.15 g ZVAL and/or 0.15 g anatase (TiO<sub>2</sub>), and 0.15 g ZVAL and/or 0.15 g rutile (TiO<sub>2</sub>) were mixed with 10 mL of gold–copper ammoniacal thiosulfate solution in 20 mL Erlenmeyer flasks at room temperature (25 °C). Note that the gold thiosulfate solution was purged with ultrapure nitrogen (N<sub>2</sub>) gas to take out all dispersed dissolved oxygen in the system as per the previous research [1], where the absence of O<sub>2</sub> in the system leads to a more significant metal recovery. The shaking amplitude was maintained at 40 mm at a frequency of 120 per minute. The residues were thoroughly washed with deionized water (18 MΩ·cm, Mill-Q<sup>®</sup> Integral Water Purification System, Merck Millipore, USA), followed by drying the residues in a conventional oven at 105 °C for 1 h and then further analysis by scanning electron microscopy with energy dispersive X-ray spectroscopy (SEM-EDX) (SEM-EDS, JSM-IT200TM, JEOL Co., Ltd., Tokyo, Japan). SEM-EDX was operated at an accelerating voltage of 15 kV, 1000× to 1500× magnification, and a working distance (WD) of 12 mm. The elemental maps were taken at 10,000 cps with 60 min time constant and high pixel resolutions of 256 × 256 (~10 min scans). Also, the solid particles were subjected to X-ray photoelectron spectroscopy (XPS) analysis using a JEOL JPS-9200 spectrometer (JEOL Ltd., Tokyo, Japan) equipped with a monochromatized Al Kα X-ray source operating at 100 W under ultrahigh vacuum (about 10<sup>−7</sup> Pa). Wide-scan and narrow-scan spectra of Au and Cu were obtained using the binding energy of adventitious carbon (285.0 eV). All XPS data were deconvoluted using JEOL Specs surf (JEOL Ltd., Tokyo, Japan) Analysis using an accurate Shirley background and a 20–80% Lorentzian–Gaussian peak model [16,17].

Simultaneously, the concentrations of gold ions suspected to remain in the barren solution were analyzed using inductively coupled plasma atomic emission spectroscopy (ICP-AES) (ICPE-9820, Shimadzu Corporation, Kyoto, Japan, with a margin of error = ±2%), and Au recovery (Au<sub>R</sub>) was calculated accordingly (see Equation (1), where Au<sub>R</sub> is the

percent Au recovery,  $Au_i$  is the initial Au concentration, and  $Au_f$  is the final Au concentration, respectively).

$$\%Au_R = \frac{[Au_i] - [Au_f]}{[Au_i]} \times 100 \quad (1)$$

### 2.3. Electrochemical Measurements

#### 2.3.1. Preparation of Aluminum Electron Mediator Working Electrodes

Previous research [1] explicitly described an improvised metal oxide/Al electrode. The working electrodes were prepared by connecting an Al metal sheet to a copper wire attached with silver conducting paste (CAS No.: 7440-22-4, Sigma-Aldrich, Kyoto, Japan) and fixing it inside a plastic mold (25 mm diameter and 10 mm height) with Technovit® non-conductive resin (Heraeus Kulzer GmbH, Hanau, Germany).

The resulting Al electrode was then exposed and polished using silicon carbide paper. Finally, the polished electrode was ultrasonically cleaned and washed several times with DI water (18 MΩ·cm, Milli-Q® Integral Water Purification System, Merck Millipore, Burlington, MA, USA).

The magnetite/Al, hematite/Al, anatase/Al, and rutile/Al working electrodes were then prepared by attaching 0.05 g of electron mediator to the surface of the Al working electrode. Comparatively, high-purity hematite, magnetite, and rutile minerals were used as working electrodes to further understand the selective cementation mechanism. Mineral specimens are shown in Figure 1 and scaled to 20 mm Japanese coins, and they were prepared similarly to the previous section above.

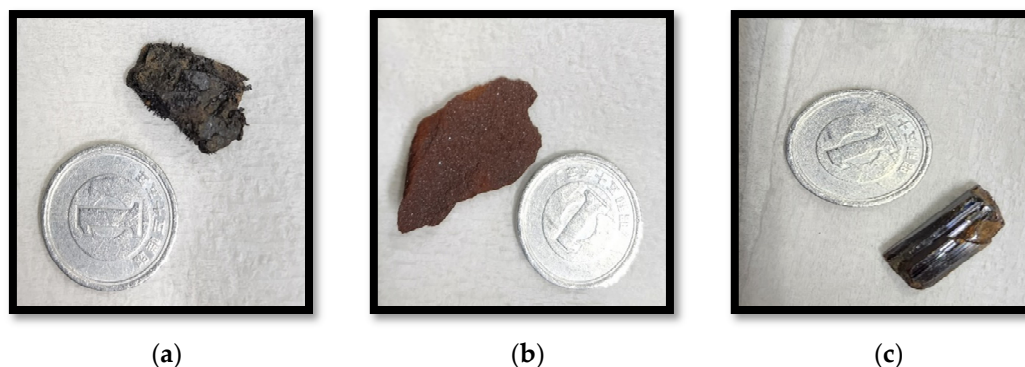


**Figure 1.** Mineral specimen used as improvised working electrode: (a) magnetite,  $Fe_3O_4$ ; (b) hematite,  $Fe_2O_3$ ; and (c) rutile,  $TiO_2$ .

#### 2.3.2. Cyclic Voltammetry Measurements

Cyclic voltammetry is a surface-sensitive technique capable of identifying the redox properties of surface-bound species by measuring the current generated by an applied potential [1,15,18]. Cyclic voltammetry, V, was conducted using a computer-driven potentiostatic electrochemical measurement (SP-300, Biologic, Seyssinet-Pariset, France) with a conventional three-electrode system to elucidate the electrochemical properties of each working electrode. In this research, CV experiments were conducted using synthetic anatase and rutile (attached to ZVAL as a working electrode) to compare their electrochemical properties from the previous research using synthetic magnetite and hematite and a  $Ag/AgCl_2$  electrode filled with saturated KCl as the reference electrode and a platinum (Pt) electrode as the counter electrode. CV measurements were conducted in anoxic conditions (without dissolved oxygen) by purging the prepared 150 mL electrolyte solution with ultrapure  $N_2$  gas (99.99%) for 45 min before electrochemical measurements. The electrolyte solution was prepared with the same conditions presented during cementation. Three electrodes were immersed in a glass cell with a water jacket before  $N_2$  purging and equilibrated at 25 °C for 30 min. In all cases, measurements were always performed after the equilibration of the working electrode to its open-circuit potential (OCP). Equilibrium means the working

electrode's measured current did not change by more than 2 mV for 60 s. The scan started from the OCP and moved towards more positive potentials at a rate of 10 mV/s up to +1.0 V, after which the sweep direction was reversed and moved towards increasingly negative potentials. The scan direction was again reversed after reaching  $-1.5$  V and then moved back to the starting position (i.e., the OCP). This entire process constituted one cycle; each measurement lasted three cycles under unstirred conditions. Triplicate measurements were performed using this technique. After this, the electrochemical properties of pure mineral specimens as working electrodes were subjected to cyclic voltammetry.

### 2.3.3. Chronoamperometry and Electrode Surface Characterization

Chronoamperometry is an electrochemical technique that applies a fixed potential to the working electrode, and current density change is recorded over time [1,15,18]. Chronoamperometry measurements were conducted using a computer-driven potentiostatic electrochemical measurement (SP-300, Biologic, Seyssinet-Pariset, France) with a conventional three-electrode system. After equilibration of each improvised working electrode to the OCP, it was polarized at a fixed potential of  $-1.0$  V (Au reduction potential) for 60 min and at constant agitation speed at 120 rpm using a magnetic stirrer, and the entire system was maintained at  $25$  °C. After the process, the working electrode was immersed in deionized water and cured in a vacuum oven at  $40$  °C for 24 h. The surfaces of all improvised working electrodes were then investigated using scanning electron microscopy with energy dispersive X-ray spectroscopy, SEM-EDX, to verify the deposited metal at the surface.

### 2.3.4. Potentiostatic Electrochemical Impedance Spectroscopy (PEIS)

Electrochemical impedance spectroscopy analysis is a powerful tool for determining the mechanism involved in an electrochemical reaction and the values of the kinetic parameters of this mechanism, and it is used for the electrical characterization of semiconducting material [19–21]. Potentiostatic EIS performs impedance measurements in potentiostatic mode by applying a sinus around a potential that can be set to a fixed value or the cell equilibrium potential. The PEIS experiments used a computer-driven potentiostatic electrochemical measurement ((SP-300, Biologic, Seyssinet-Pariset, France) with a conventional three-electrode system. After equilibration of each improvised working electrode to the OCP after 60 min, it was then polarized at biased potential from  $1.0$  V to  $-1.5$  V with  $0.1$  V interval in the  $200$ – $100$  Hz frequency range, and the entire system was maintained at  $25$  °C. The resulting impedance spectroscopy data were then analyzed with an appropriate equivalent circuit using “Z-Fit” analytical software embedded in the SP-300 (Biologic, Seyssinet-Pariset, France) as an analytical tool interface to calculate the resulting EIS data.

### 2.3.5. Staircase Potentiostatic Electrochemical Impedance Spectroscopy (Mott–Schottky Plot)

SPEIS is a powerful technique designed to perform successive impedance measurements (on a whole frequency range) during a potential scan. The main application of these techniques is to study the electrochemical reaction kinetics along voltaperometric curves in analytical electrochemistry. This technique consists of a staircase potential sweep ( $1.0$  V to  $-1.5$  V). Impedance measurements concerning different frequencies are performed in each potential step. For all these applications, a Mott–Schottky plot ( $1/C_2$  vs. Ewe) can be displayed, and a unique linear fit is applied to extract the semiconductor parameters, such as the flat band potential [22–26].

In this experiment, the impedance of different electron mediators (high-purity magnetite, hematite, and rutile) was measured at bias potentials ranging from  $+1.0$  V to  $-1.5$  V (versus Ag/AgCl) in  $0.1$  V increments, and 60 min was used to allow equilibration at each new potential. The frequency range was performed at  $20$  kHz to  $1$  kHz. The Mott–Schottky plot was automatically plotted in the analytical software embedded in the SP-300 (Biologic, France) and flat band potential can be determined using BioLogic EC-Lab V11.10 software.

#### 2.4. UV-Vis Spectroscopy (Direct Bandgap Measurement)

The bandgap represents the minimum energy difference between the valence band's top and the conduction band's bottom. UV-Vis spectroscopy, which measures light absorption as a function of wavelength, gives information on electronic transitions occurring in semiconductor materials as a function of incident light wavelength and thus acts as a tool to estimate the optical band gap [27]. The optical band gap is approximated to the electronic band gap, defined as the energy difference between the conduction band maximum and the valence band minimum. Reference UV-Vis potentiostatic electrochemical measurement spectra (background measurement) were measured using a glass tube with ultra-pure water. The UV-Vis absorbance spectra of the solid samples were measured by ultrasonically dispersing the particles in  $\text{NH}_4/\text{NH}_3$  solution (pH 9.5) in the glass tube following the measurement using a UV-Vis V-630 spectrophotometer (Jasco, Easton, MD, USA). This technique was operated in the 1000 nm to 190 nm wavelength range (deuterium lamp: 190–350 nm; halogen lamp: 330–1000 nm) at a 12,000 nm/min measurement rate.

### 3. Results and Discussion

#### 3.1. Recovery of Gold Ions from Ammonium Thiosulfate Solution

As already reported in previous research, when iron oxides (hematite and magnetite) were used as an electron mediator for the cementation of metals from gold–copper ammoniacal thiosulfate solutions using aluminum as an electron donor, selective deposition of gold occurred, and copper cementation was limited. Different semiconductive materials were used to investigate further the effect of semiconducting materials on the recovery of copper in an ammoniacal thiosulfate medium to understand the relative effect on the difference in metal recovery. Figure 2 shows the percent Au and Cu recovery of the different electron mediators after the cementation process in (a) a single system (zero-valent aluminum, activated carbon, magnetite, hematite, anatase, and rutile) and (b) a binary system using Al as electron donor and different electron mediators. The results of cementation experiments in a single system are presented in Figure 2a; noticeably, in a single system, all constituents were able to recover gold and copper: 38.2% Au/18.9% Cu for aluminum, 30.1% Au/6.1% Cu for activated carbon, 22.1% Au/0% Cu for magnetite, 24.2% Au/0% Cu for hematite, 32.5% Au/16.4% Cu for anatase, and 26.1% Au/12.4% Cu for rutile. Comparatively,  $\text{TiO}_2$  (anatase) and  $\text{TiO}_2$  (rutile) have been shown to have higher copper recovery compared to other electron mediators, having 16.4% Cu and 12.4% Cu, respectively, as presented in Figure 2a.

In a binary system, as shown in Figure 2b, gold recovery was significantly increased using aluminum as an electron donor, which was further validated using other semiconductive materials using  $\text{TiO}_2$  (anatase) and  $\text{TiO}_2$  (rutile), having 92.6% and 93.5% gold recovery, respectively. The results also obtained significant differences concerning copper recovery, around 62.2% and 66.9% for anatase and rutile, respectively. This further suggests that the semiconductive property of electron mediators has influenced the increase in copper recovery. Table 2 presents some semiconductive properties of electron mediators used in this research.

**Table 2.** Some semiconductive properties of electron mediators [22].

Semiconductors	Semiconductivity Bandgap [eV]	Semiconductivity Type
Activated Carbon (AC)	3.5	n-type/p-type
Hematite, $\text{Fe}_2\text{O}_3$	1.9–2.2	n-type
Magnetite, $\text{Fe}_3\text{O}_4$	0.9–1.9	n-type
Anatase, $\text{TiO}_2$	3.0	n-type
Rutile, $\text{TiO}_2$	3.3	n-type

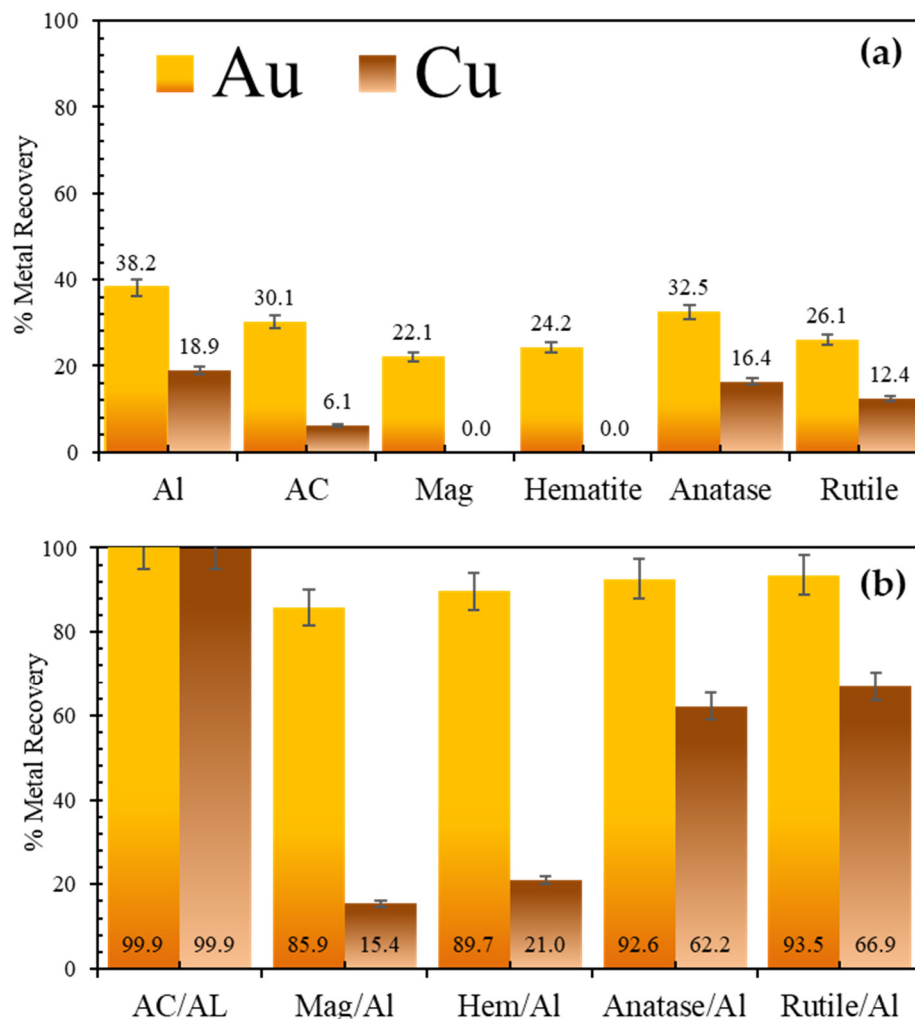


**Figure 2.** Percent metal recovery using different electron mediators after cementation process in (a) single system and (b) binary system.

Given the information in Table 2, we can infer that the bandgap has something to do with increased copper recovery in a binary system. The greater the bandgap, the higher the copper recovery. Although many researchers have reported the semiconductive properties of some metal oxides, the values of these properties depend on many factors, such as the material's particle size and pH and the crystal structure of the materials (50–53). For this reason, further electrochemical experiments were conducted to evaluate the semiconductive properties of the metal oxides used in this research, presented in the following sections.

SEM-EDX spectroscopy was conducted further to confirm the presence of metal deposition after cementation experiments. Figure 3 presents the scanning electron microscopy profile (analyzed using elemental mapping and point EDS) of the different electron mediators in a single system: (A) magnetite, (B) hematite, (C) anatase, and (D) rutile. It can be observed that fine particles of electron mediators (grey objects in backscattered electron (BSE) photomicrographs) were spontaneously covering the cemented metal (bright objects in BSE photomicrographs), which can further be detected using the point analysis technique and elemental mapping. Comparatively, using iron oxides as electron mediators (Figure 3A,B), the bright particles detected were assigned to gold particles only; no copper was detected compared to titanium oxides (Figure 3D) as presented on its corresponding elemental mapping and point EDS analysis.

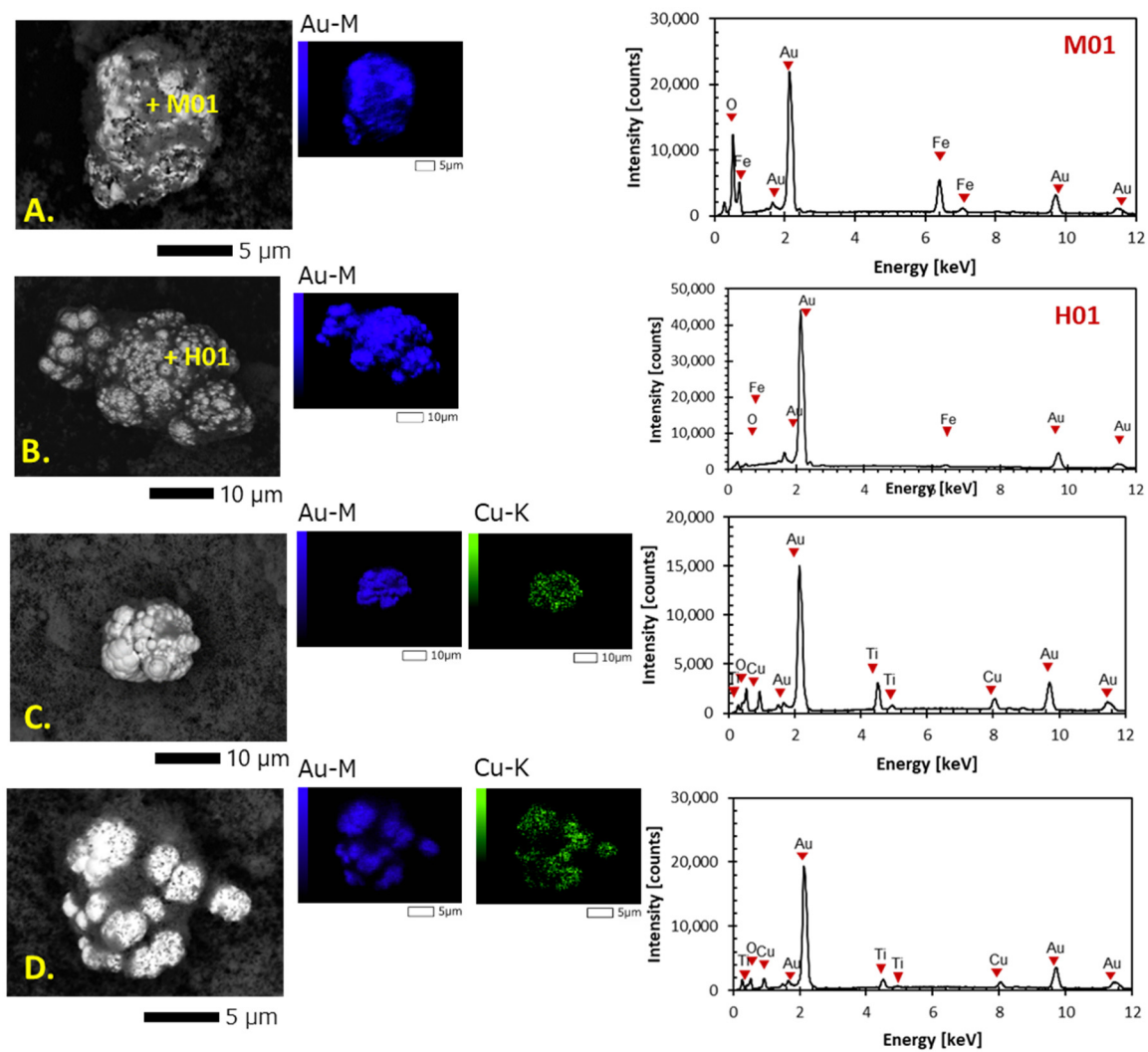


**Figure 3.** SEM-EDX profile of cemented gold in different semiconductive materials in single system: (A) magnetite, (B) hematite, (C) anatase, and (D) rutile.

Also, Figure 4 presents the SEM-EDX profile of the electron mediators in the binary system using zero-valent aluminum as an electron donor. In all photomicrographs, the cemented bright particles were all detected along with spherical-shaped particles, which is the oxidized aluminum oxide layer observed in Figure 4a–d. The backscattered electron (BSE) photomicrographs and their corresponding elemental mapping and point EDS analysis confirmed that all electron mediators could cement gold. Noticeably, copper was also cemented, but its intensities are much lower in iron oxides, averaging around 5000 cps, compared to titanium oxides ranging from 5000 cps to 20,000 cps. The results of the SEM-EDX analysis further suggest that when we used iron oxides as electron mediators and zero-valent aluminum as an electron donor, they presented better selectivity than titanium oxides.

Furthermore, X-ray photoelectron spectroscopic analysis (XPS) was conducted to validate the presence of cemented metals further using the different electron mediators in single and binary systems. XPS was conducted using a JEOL JPS-9200 spectrometer (JEOL Ltd., Tokyo, Japan) equipped with a monochromatized Al K $\alpha$  X-ray source operating at 100 W under ultrahigh vacuum (about 10<sup>−7</sup> Pa). A wide-scan (Figures 5 and 6) and narrow-scan (Figures 7 and 8) spectrum of oxygen (O 1s) and carbon (C 1s) were obtained and corrected using the binding energy of the adventitious carbon (285.0 eV). All XPS spectra

were deconvoluted with XPSPEAK version 4.1 using an accurate Shirley background and a 20–80% Lorentzian–Gaussian peak model [16,17].

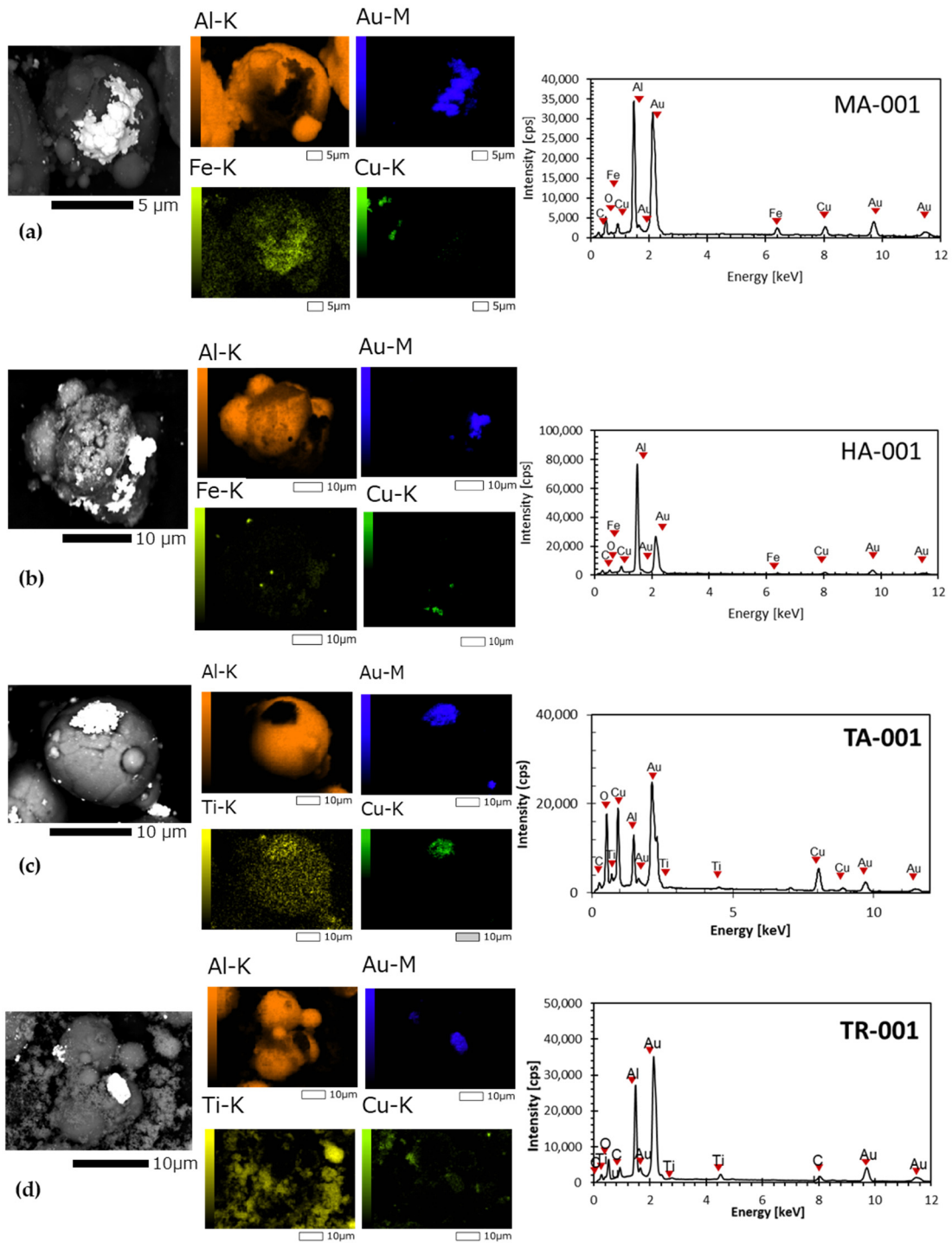


**Figure 4.** SEM-EDX profile of cemented gold using different semiconductive material in binary system: (a) magnetite/Al, (b) hematite/Al, (c) anatase/Al, and (d) rutile/Al.

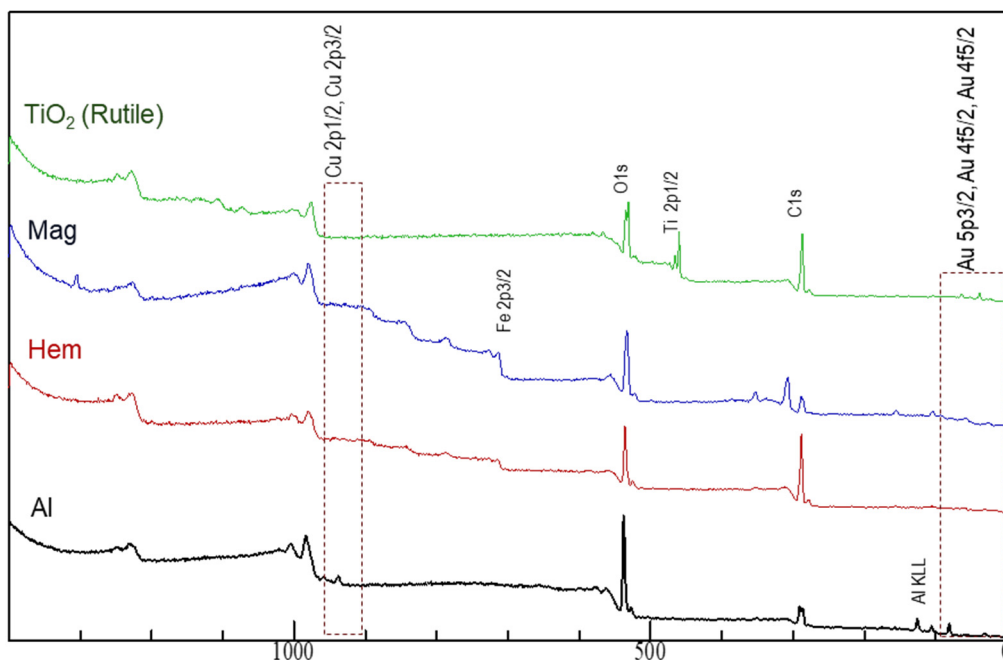


**Figure 5.** XPS wide-scan spectra of selected electron mediators (rutile, magnetite, hematite) and zero-valent aluminum (Al) in single system.

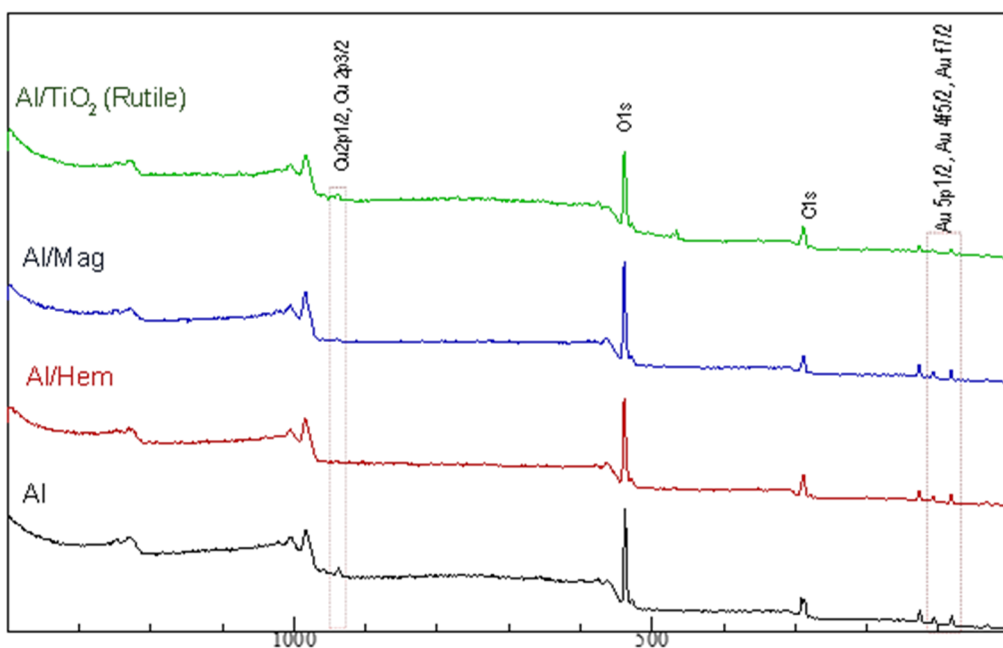


**Figure 6.** XPS wide-scan spectra of selected electron mediators (rutile, magnetite, hematite) and zero-valent aluminum (Al) in binary system.

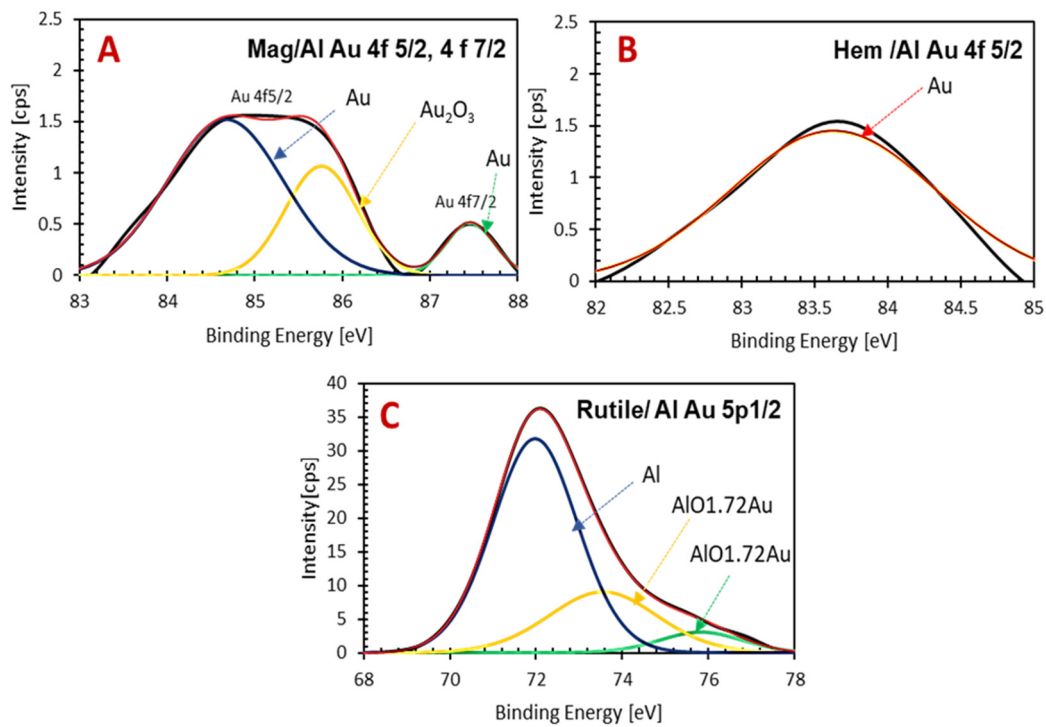


**Figure 7.** XPS Au narrow scan of selected electron mediator/electron donor system: (A) magnetite/Al, (B) hematite/Al, and (C) rutile/Al.

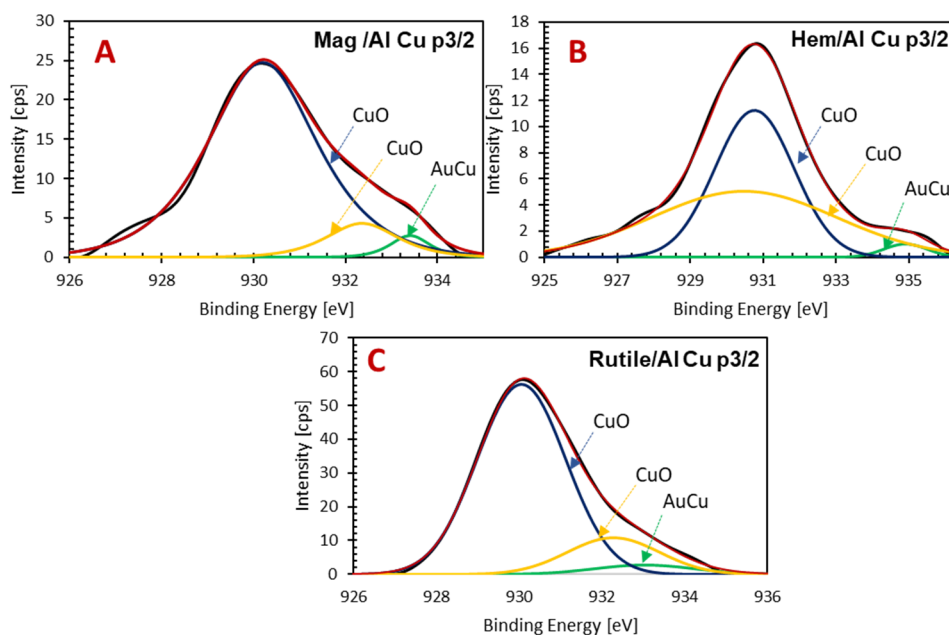


**Figure 8.** XPS Cu narrow scan of selected electron mediator/electron donor system: (A) magnetite/Al, (B) hematite/Al, and (C) rutile/Al.

Figures 5 and 6 present the XPS wide spectra of selected electron mediators (rutile, magnetite, and hematite) and compare them to zero-valent aluminum in single and binary systems. The results revealed that XPS spectra of single and binary systems could detect the presence of Au peaks at different energy levels: Au 5p<sub>3/2</sub>, Au 4f 7/2, and Au 4f 5/2 detected at binding energy range 68–85 eV. On the other hand, in a single system, using magnetite and hematite presents no significant copper peaks compared to rutile (slightly forming an amorphous-like peak) and aluminum was detected at the binding energy range

of 926–925 eV for Cu 2p<sub>1/2</sub> and Cu 2p<sub>3/2</sub>, which is in agreement with the results of metal recovery upon the cementation process where no copper was recovered when we used iron oxides as the electron mediator.

Also, in a binary system, we can observe clearly that copper was detected in all systems; comparing the XPS spectra of aluminum to the electron mediator/electron donor system, we can infer that the copper detected using iron oxides was made possible due to the presence aluminum, which acts as an electron donor and as a reductant of copper simultaneously, which agrees with the results presented in the Figure 4a,b SEM-EDX elemental mapping, where the illuminated copper was detected separately at the surface of the aluminum, while the titanium oxides were able to cement Au and Cu in exact position (Figure 4c,d). A narrow scan was conducted at the specified binding energy range of gold and copper to determine the wide-scan spectra exact energy positions and detailed components. The XPS narrow-scan spectra are presented in Figures 7 and 8.

Deconvoluted narrow XPS spectra of gold are presented in Figures 7 and 8. The scan range was based on the wide-scan XPS spectra, where the rutile/Al binary system was shown to have a gold peak at a binding energy range around 68–78 eV, which belongs to the Au 5p<sub>1/2</sub> electron orbital, while iron oxides have gold peaks at a binding energy range of 82–88 eV, which belongs to the Au 4f<sub>5/2</sub> and Au 4f<sub>7/2</sub> electron orbitals. The results revealed that magnetite/Al detected three significant peaks centered at 84.6 eV, 85.7 eV, and 87.5 eV, which belong to Au, Au<sub>2</sub>O<sub>3</sub>, and Au, respectively. Also, hematite/Al obtained only one gold peak centered at 83.6 eV, which belongs to elemental Au, while for rutile/Al, two major gold peaks belonging to AlO<sub>1.72</sub>Au were obtained, centered at 73.7 and 75.8 eV.

On the other hand, the deconvoluted narrow XPS spectra of copper were the same in all binary system constituents, where the narrow scan was focused on a binding energy range of 926–936 eV. The results obtained three significant peaks for all binary system constituents. Binding energies centered at 929–930 eV, 931–932 eV, and 933–934 eV were assigned to Cu, CuO, and AuCu, respectively. The results concerning XPS copper intensities agree with those obtained using the SEM-EDS point analysis shown in Figure 4, where titanium oxide as an electron mediator obtained significantly higher copper intensities compared to iron oxides. This research further suggests that SEM-EDX and X-ray photoelectron spectroscopic analysis can confirm the selective cementation of iron oxide to gold upon cementation in copper ammoniacal thiosulfate medium.

### 3.2. Electrochemical Experiments

Figure 9 illustrates the cyclic voltammogram spectra (Figure 9A) and narrow reductive scan voltammogram spectra (Figure 9B) of titanium oxide (anatase/rutile)/Al working electrodes using gold and copper electrolytes. The previous chapter discusses the galvanic interaction between ZVAL and iron oxides and compares it to an Al/AC working electrode; it was reported that using iron oxides as electron mediators facilitates the selective cementation of gold [1]. Like the voltammogram generated using the AC/Al working electrode, two reduction peaks were observed. When the potential sweep moves towards a more negative potential, a “shoulder-like” peak was observed around −0.7 V for the anatase/Al and rutile/Al working electrode, which is assigned to reducing copper ions. Furthermore, around −1.0 V, a “shoulder-like” peak was observed and assigned to reducing gold ions. These results further validate that gold and copper can be reduced using a titanium oxide/Al working electrode, suggesting that it does not possess selective cementation properties. To further understand if titanium oxide facilitates the cementation of gold and copper, the same procedure was conducted using a high-purity mineral specimen as a working electrode. Its corresponding electrochemical profile is illustrated in Figure 10.

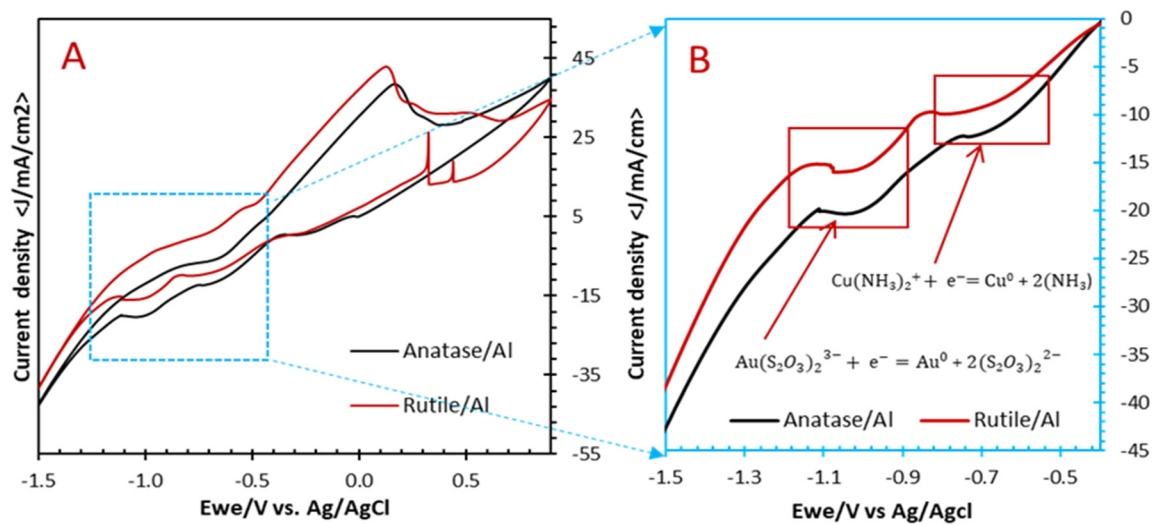


Figure 9. Cyclic voltammogram profile of titanium oxide (anatase and rutile)/Al working electrode.

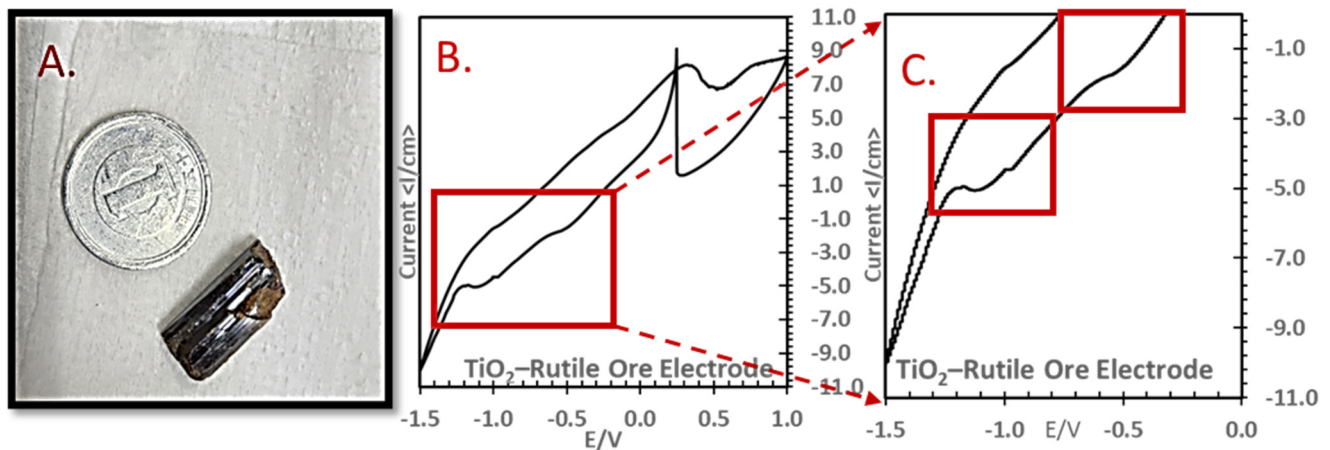
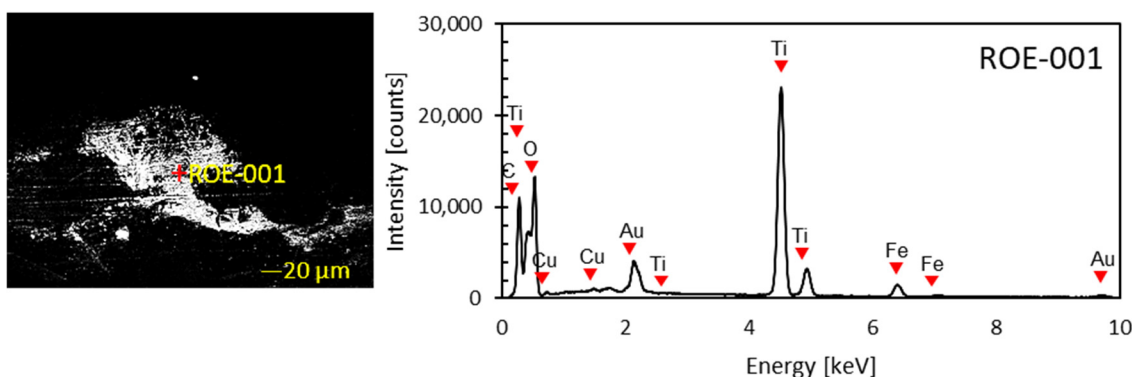


Figure 10. Electrochemical profile using rutile crystal: (A) rutile crystal specimen, (B) cyclic voltammogram, (C) narrow reductive scan.

Figure 10B demonstrates the cyclic voltammogram of rutile crystal around 20 mm subjected to a potential scan from 1.0 V to  $-1.5$  V versus AgCl. Its narrow potential scan is illustrated in Figure 10C. The results further validate that the use of titanium oxide alone can reduce  $\text{Au}(\text{S}_2\text{O}_3)_2^{3-}$  species into metallic gold as well as  $\text{Cu}(\text{NH}_3)_2^+$  species into metallic copper; the reduction potential peaks were observed around  $-1.1$  V and  $-0.5$  V for gold and copper, respectively. These results further suggest that the electron mediator facilitated the cementation using titanium oxide and that the cementation of gold and copper was enhanced by using an electron donor, which is, in this case, ZVAL.

Figure 11 presents the SEM-EDX profile of a rutile working electrode after chronoamperometry subjected to a fixed potential of  $-1.1$  V for 1 h in a gold–copper ammoniacal thiosulfate medium. The results further validate that gold and copper were detected. These results further supplement the claim that the electron mediator plays a vital role in the selective cementation of electron mediators.



**Figure 11.** SEM-EDX profile of rutile crystal working electrode after cementation.

PEIS permits us to identify and analyze the contributions of different parameters in each frequency and temperature domain, such as the impedance and the bulk capacitance. For this purpose, the PEIS data simulated by an equivalent circuit are presented using a Nyquist plot. In the Nyquist plot, the modulus  $|Z|$  and the phase angle define the position of each frequency-dependent data point in a complex plane. The Bode plot plots  $|Z|$  and phase angle against the modulation frequency. This maximum of “ $-\text{Im}(Z)$  [ $\Omega$ ]” (imaginary impedance) corresponds to the inflexion point in the “ $\text{Re}(Z)$  [ $\Omega$ ]” (real impedance). Otherwise, the Nyquist representation is characterized by impedance spectra intercepting the actual impedance.

The behaviors in the Nyquist plot, as shown in Figure 12 for our representative material and a representative temperature of 25 °C and a bias potential at 0 V maintained at pH 9, indicate the contribution of only one process at maximum frequency. It can be noticed that the Nyquist plot (inset figure) is not a full semi-circle. It is a depressed semi-circular arc whose center lies below the real impedance axis, suggesting the poly dispersive non-Debye relaxation type in our case. In this situation, constant phase elements (CPE) must be used in addition to resistors and capacitors to describe the equivalent circuit, which will be discussed later, to provide a complete picture of the system. Also, the lack of observation of peaks in the frequency domain ( $2-1 \log$  frequency, KHz) suggests that the observed single peak in the plots of imaginary impedance represents the grain boundary component [24–26].

Also, single semi-circular arcs are observed in Figure 12 and are related to the dominance of the contribution of the grain boundary process in the considered temperature and frequency ranges. To understand and extract meaningful information from the EIS data presented in Figure 13, an equivalent circuit model must be fitted that combines fundamental elements such as resistors, capacitors, inductors, constant phase elements, and diffusion elements.

The process of fitting the data by considering different electrical circuits, depending on the applied voltage domain, has been described by Bredar et al., 2020 [27–29]. An essential feature of this EIS diagram is the linear increase in impedance observed in the midfrequency range; this can be attributed to Warburg diffusion. As such, Figure 13 shows the selected equivalent circuit for analyzing data generated from EIS experiments; EC-Lab V.11.10 ZFit-Bio Logic Software suggested this equivalent circuit. This model has been used to explain the resistance to charge transfer between metal oxides and conductive substrates, often called contact resistance. This circuit modifies Randle’s circuit, where a Warburg diffusion (ZW) term has been included in series with the charge transfer resistance. This arrangement describes the physical reality of electroactive species’ diffusion to the electrode’s surface, where they undergo oxidation or reduction via charge transfer.

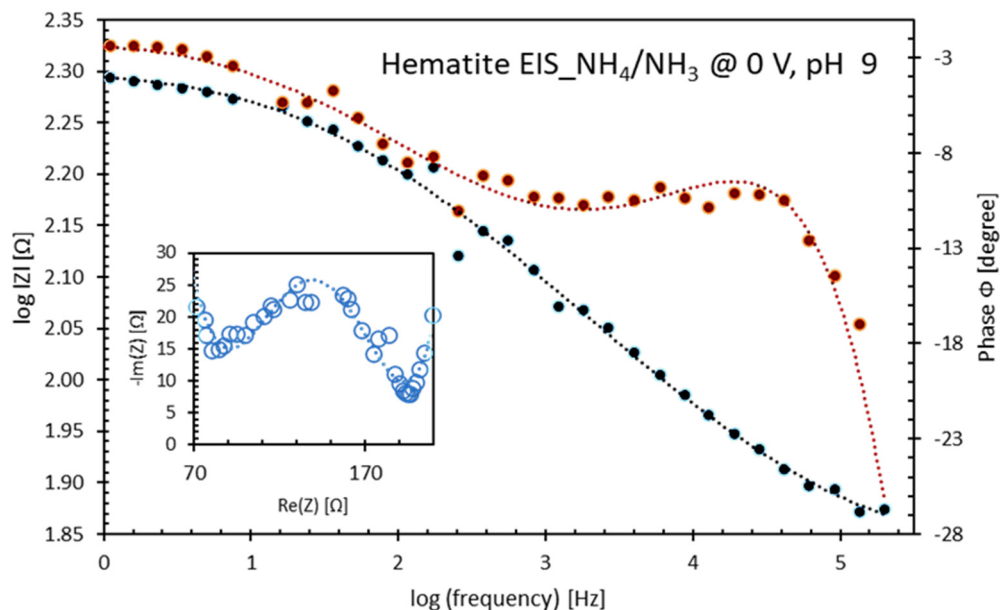


**Figure 12.** Representative electrochemical impedance spectroscopic analysis profile of a hematite working electrode at applied bias potential of 0 V and constant pH 9 at 25 °C.

**Impedance**

$$Z(f) = R_1 + \frac{R_2}{1 + j2\pi f R_2 C_2} + \frac{\sqrt{2} \sigma_3}{\sqrt{j2\pi f}}$$

**Nyquist Diagram (-Im(Z) vs. Re(Z))**

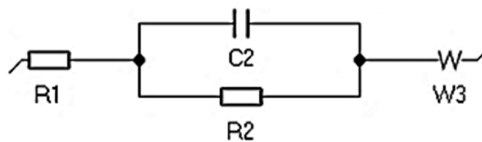
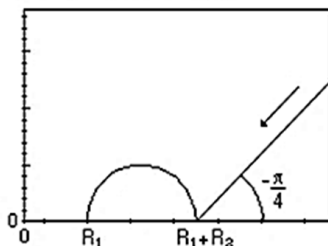


**Figure 13.** Equivalent circuit used to analyze the EIS profile of different working electrodes using EC-Lab V11.10 ZFit-Bio Logic software.

To identify the contribution of bias voltage, Figure 14 compares the Nyquist plots for the different working electrodes using NH<sub>4</sub>/NH<sub>3</sub> buffer solution (pH 9) at five representative bias voltages at 1.0 V and 0 V versus the Ag/AgCl reference electrode. In these curves, a maximum of imaginary impedance was observed at different bias voltages applied, specifically when 1.0 V was applied, indicating the displacement of the peak towards higher frequencies with increasing voltage.

To further understand the behavior of metal oxides as electron mediators, EIS was conducted using gold ions and copper ions as electrolytes in an ammoniacal thiosulfate medium. The EIS profile of each electrode is illustrated in Figure 15, represented in Nyquist plots.

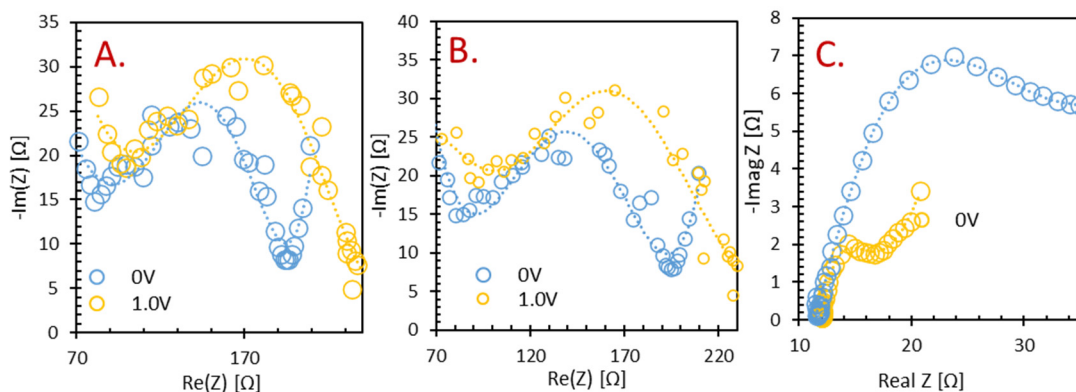


**Figure 14.** EIS profiles of different working electrodes, represented using Nyquist plots, subjected to 1.0 V and 0 V using  $\text{NH}_4/\text{NH}_3$  buffer solution (pH 9) at 25 °C. (A) Magnetite. (B) Hematite. (C) Rutile.

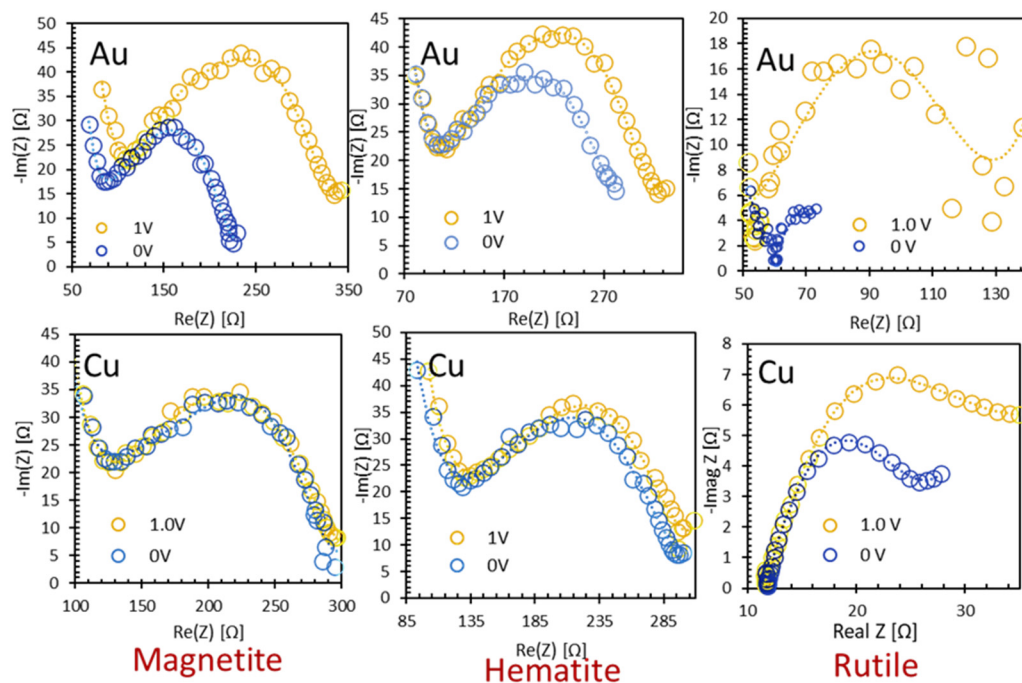


**Figure 15.** EIS profiles of the different working electrodes using metallic electrolytes (pH 9) subjected to different bias voltages from 1.0 V to 0 V and represented in Nyquist plots.

The results of potentiostatic impedance spectroscopy were calibrated by applying a bias potential from 1.0 V to 0 V; we can observe that the charge transfer resistance (semi-circle) of all working electrodes decreased, as shown in Figure 15, when using gold ions only as the electrolyte. These results further suggest that electrodes could develop a solid–liquid interface that affects the electron transfer more favorably and becomes a conducting surface when approaching a more negative potential.

On the other hand, the PEIS Nyquist plot also suggests that when using copper electrolytes and when using hematite and magnetite as working electrodes, the contact resistance of both electrodes did not develop any significant change when bias potential was applied from 1.0 V to 0 V, which is contrary to the Nyquist plot generated using rutile as the working electrode.

Also, as the potential approaches 0 V, the semi-circle becomes more well defined; this indicates that the ionic resistance for  $\text{Au}^+$  decreases in all metal oxide electrodes, while

$\text{Cu}^+$  migration through the solid–electrolyte interface decreases only when using the rutile electrode.

Overall, potentiostatic electrochemical impedance spectroscopic analysis, represented by Nyquist plots, demonstrated the ability of impedance in the form of charge transfer resistance to differentiate the semiconductive behavior of metal oxides (magnetite, hematite, and rutile) while considering the unique contributions of the different metallic electrolytes in different applied bias potentials.

### 3.3. Mott–Schottky Plot

SPEIS was conducted by applying a staircase potential sweep from a positive to negative potential (1.0 V to  $-1.5$  V) versus the Ag/AgCl reference electrode. The Mott–Schottky plot was automatically plotted in analytical software embedded in SP-300 (Biologic, Seyssinet-Pariset, France) and flat band potential can be determined using BioLogic EC-Lab V11.10 software, as illustrated in Figure 16.

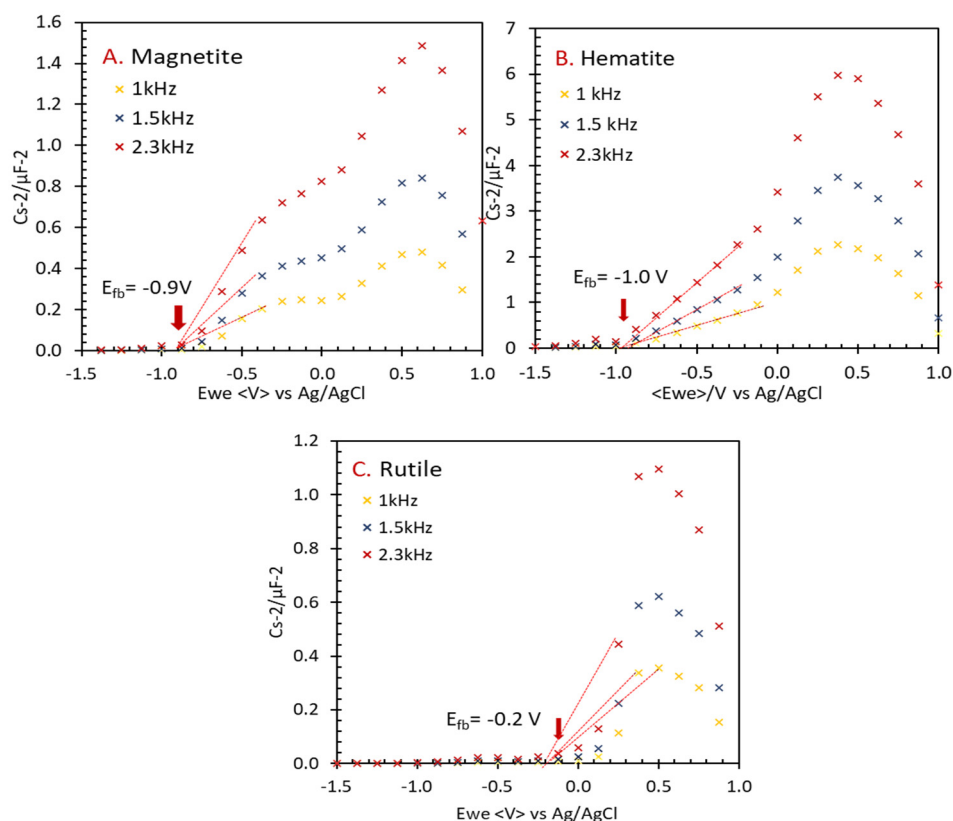


**Figure 16.** Mott–Schottky plots of different metal oxide ore specimens performed in  $\text{NH}_4/\text{NH}_3$  buffer solution. (A) Magnetite. (B) Hematite. (C) Rutile.

Figure 16 illustrates the Mott–Schottky plots for (A) magnetite, (B) hematite, and (C) rutile in  $\text{NH}_4/\text{NH}_3$  buffer solution (pH 9.5). The plots were acquired in a potential sweep from 1.0 V to  $-1.5$  V in a frequency ranging from 200 kHz to 1 kHz, but only lower frequencies (1 kHz, 1.5 kHz, and 2.3 kHz) are represented to refine the presentations.

When the applied potentials approach is more negative, around 0.5 V to  $-0.9$  V, 0.5 V to  $-1.0$  V, and 0.5 V to  $-0.2$  V, the plots have a positive slope for magnetite, hematite, and rutile, respectively. More than that of 0.5 V, the Mott–Schottky plots start to decrease, suggesting that no direct correlation between the semiconducting properties can be established in this region. On the other hand, the positive slope of the Mott–Schottky plot at lower potentials in the passive region confirms that magnetite, hematite, and rutile behave like n-type semiconductors [20]. To recognize whether a linear dependence exists over a specific potential range and thus obtain a reliable estimation, a limited linear region at the

potentials was used to estimate the flat band potential using the BioLogic EC-Lab V11.10 software. The results obtained different flat band potentials,  $-0.9$  V,  $-1.0$  V, and  $-0.2$  V, for magnetite, hematite, and rutile, respectively.

### 3.4. Direct Bandgap

This technique allows us to understand the optical and electronic properties of the investigated semiconductors, such as magnetite, hematite, and rutile. In this research, the band gap ( $E_g$ ) energy of the semiconductor being used is focused to be quantitatively determined. The band gap energy of a semiconductor describes the energy needed to excite an electron from the valence band to the conduction band. Accurately determining the band gap energy is crucial in predicting the semiconductors' photophysical and photochemical properties. The band gap energy can be determined using the UV-Vis spectra between the absorbance and corresponding UV light wavelength and converting it to a Tauc's plot. The Tauc method assumes that the energy-dependent absorption coefficient  $\alpha$  can be expressed in the following equation:

$$\alpha h\nu^{1/\gamma} = B(h\nu - E_g) \quad (2)$$

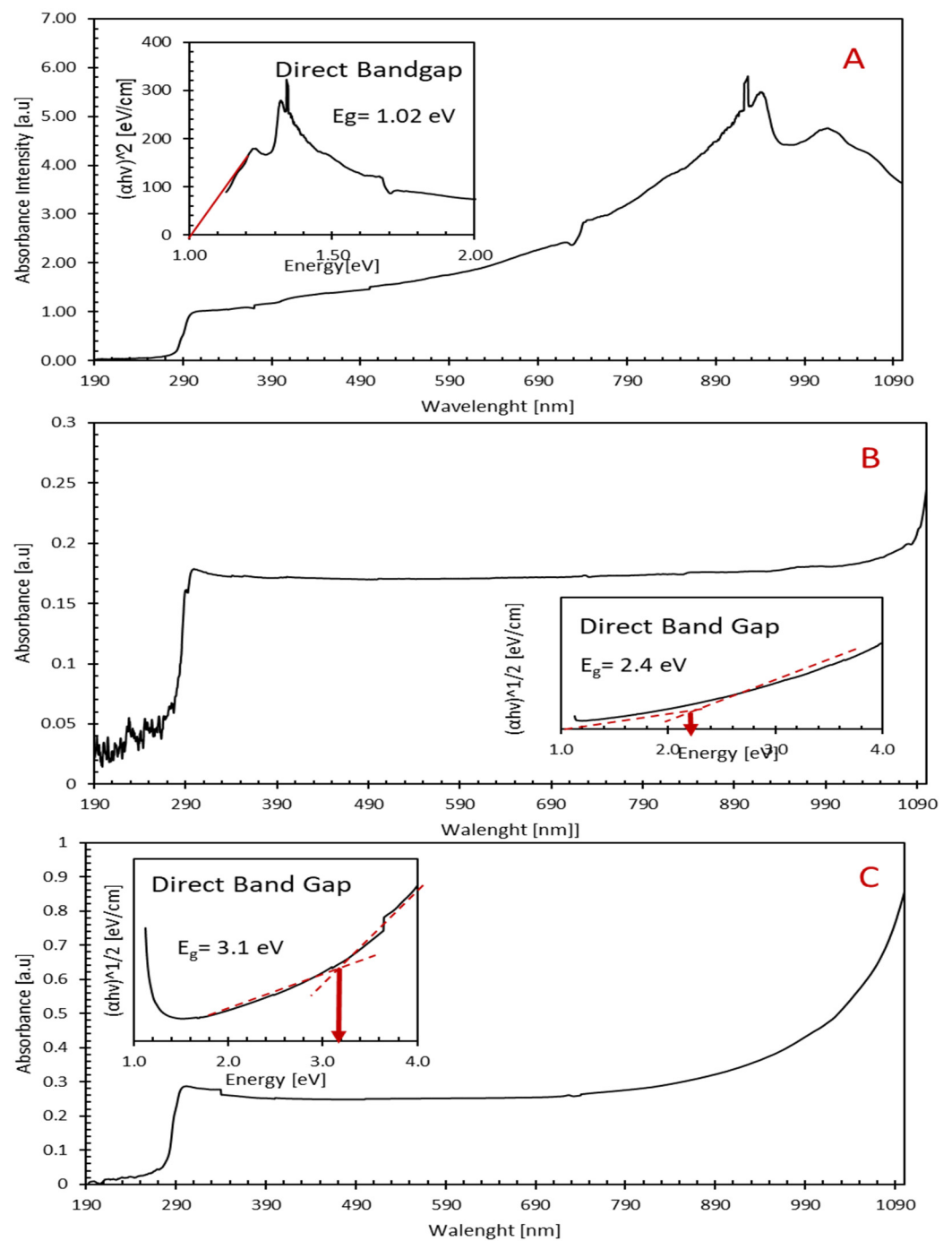
where  $h$  is the Planck constant,  $\nu$  is the photon's frequency,  $E_g$  is the band gap energy, and  $B$  is a constant. The  $\gamma$  factor depends on the nature of the electron transition and is equal to  $1/2$  or  $2$  for the direct and indirect transition band gaps, respectively [22–25].

Figure 17 shows the absorbance spectra of the different semiconductors transformed according to Equation (2) and plotted against the photon energy. The region showing a steep, linear increase of light absorption with increasing energy is a characteristic of an n-type semiconductor. The X-axis intersection points of the linear fit of the Tauc plot give an estimate of the band gap energy.

The Tauc plot is plotted in the inset figure of the UV-Vis spectra of the different semiconductors, as illustrated in Figure 17. Configuring interpolation of the linear portion of the Tauc's plot, the band gap energy was estimated to be 1.02 eV, 2.4 eV, and 3.2 eV for magnetite, hematite, and rutile, respectively. Evaluating the results given by electrochemical impedance spectroscopy and spectrophotometric analysis, the electronic band structure of the semiconductors can now be understood, as shown in Figure 18.

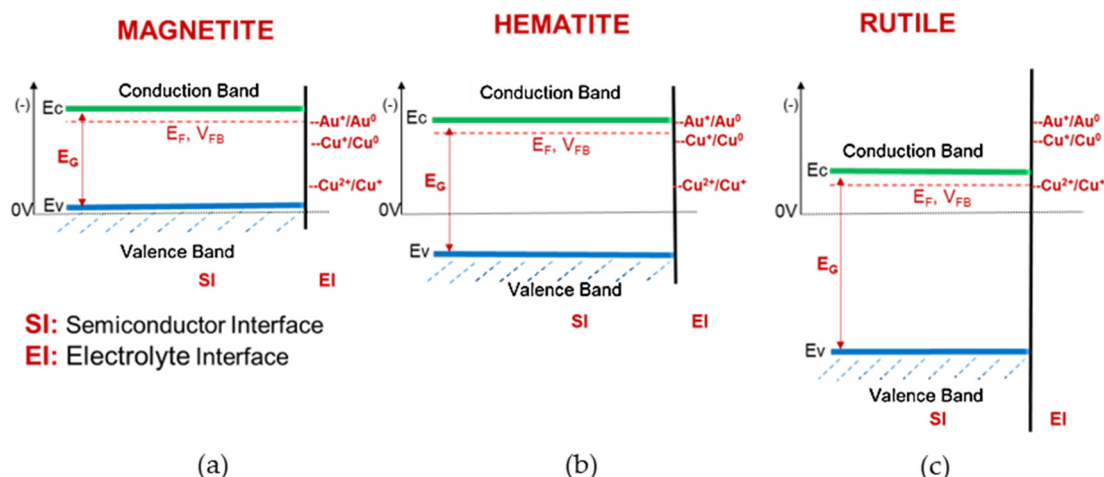
In the schematic diagram illustrated in Figure 18, two interfaces are shown in each figure. The first is the semiconductor interface (left side), where the conduction band ( $E_c$ ), valence band ( $E_v$ ), flat band potential ( $V_{fb}$ ), energy Fermi level ( $E_f$ ; red line below the conduction band edge), and the energy band gap ( $E_g$ ) edges are shown. Also, in the electrolyte interface (right side), the reduction potential edges are pinned where  $Au^+$ ,  $Cu^{2+}$ , and  $Cu^+$  are the reduction potentials at  $-1.0$  V,  $-0.8$  V and  $-0.2$  V, respectively.

Figure 18 describes the energy band diagram when a flat band structure is realized. When a flat band structure is realized, the bottom edge of the conduction band ( $E_c$ ) and the top edge of the valence band ( $E_v$ ) do not depend on the position (distance from the solid surface). They are horizontally distributed in the bulk solid phase. The flat band potential corresponds to the Fermi level of this state ( $E_f$ ) [30]. The Fermi level in the diagram corresponds to electrode potential. As already discussed, the linear positive slope at the higher potential region in the M-S plot (Figure 16) indicates that the material is an n-type semiconductor, which is, in this case, the Fermi level of the semiconductor, and the  $E_f$  sits just below the conduction band edge ( $E_c$ ). These results are considered to configure Figure 18; i.e., the position of the  $E_c$  is assumed to be the same as that of the observed flat band potentials of magnetite ( $-1.0$  V), hematite ( $-0.9$  V), and rutile ( $-0.2$  V). The position of the  $E_v$  was decided from the observed energy band gap of the materials (1.1 V for magnetite, 2.4 V for hematite, and 3.1 V for rutile).



**Figure 17.** UV-Vis spectroscopy spectra of the different semiconductors and corresponding Tauc's plots (inset of the UV spectra) of (A) magnetite, (B) hematite, and (C) rutile.

Note that in the case of iron oxides like magnetite and hematite, the reduction potential of  $\text{Au}^+$  ( $-1.0$  V) is close to that of the bottom edges of the conduction band ( $E_c$ ), while the reduction potentials of  $\text{Cu}^+$  and  $\text{Cu}^{2+}$  are far from the  $E_c$ . The reduction potentials of  $\text{Cu}^+$  and  $\text{Cu}^{2+}$  are positioned in the energy levels of the band gap of magnetite and hematite, where the electrons cannot be present in the solid phase. On the other hand, in the case of rutile, the redox potentials of  $\text{Cu}^+$  and  $\text{Cu}^{2+}$ , as well as  $\text{Au}^+$ , are higher than the  $E_c$ . This result means that the reduction potential of these metal ions is positioned at the conduction band level of rutile, where electrons can be present in the solid phase. These differences in the energy band diagrams among the three metal oxides may cause a difference in the selective deposition of metals. Details will be discussed in the next section.



**Figure 18.** Schematic energy band diagrams for the semiconductor–electrolyte interface (SEI) for (a) magnetite, (b) hematite, and (c) rutile.

Furthermore, this further suggests that electrochemical impedance spectroscopy analysis is in agreement upon analyzing the corresponding energy band diagrams of the semiconductors, where hematite and magnetite demonstrated a Nyquist plot indicating a decreased charge transfer resistance and that a semi-circular arc was observed at low frequencies using gold electrolytes upon approaching negative potentials; this can be attributed to a lower band gap and minimal Fermi level that amplifies favorable electron transfer in the solid–electrolyte interface, which explains why copper did not develop a decrease in charge transfer resistance when approaching more negative potentials [27–29].

### 3.5. Proposed Selective Cementation Mechanism

In the previously reported cementation model [1], the galvanic cementation method using ZVAL as an electron donor and iron oxides as an electron mediator was described, and it was found that selective deposition of Au from  $\text{Cu}^{2+}$ - $\text{Au}^+$  ammoniacal thiosulfate solutions occurs, and various experimental methods, including cementation experiments, surface analysis, and electrochemical experiments, carefully confirmed this. Gold was deposited on the iron oxide surface, but copper deposition was limited. The reduction potentials of the copper ions are more positive than the gold ions in the solutions, implying that the reduction (or cementation) of copper ions is thermodynamically easier than gold ions. However, this suggests that simple thermodynamic considerations cannot interpret the mechanism of the selective deposition of gold. In this section, based on the energy band diagram established in the last section, the mechanism of selective deposition of gold from  $\text{Cu}^{2+}$ - $\text{Au}^+$  ammoniacal thiosulfate solution using iron oxide (magnetite and hematite) as electron mediator with ZVAL as electron donor is discussed.

Figure 19a shows the energy band diagram when a positive potential is applied to an n-type semiconductor electrode. When the applied electrode potential is more positive than the flat band potential, the Fermi level in the energy diagram is shifted down from the flat band potential. As a result, the  $E_v$  and  $E_c$  bend like in Figure 19a; i.e., the energy level is lower at the solid bulk phase and higher at the surface. Because of the bending, electrons in the conducting band move from the solid surface (higher energy level) to the solid bulk phase (lower energy level). This bending causes the lack of electrons near the surface of the solid electrode, and the surface layer formed by this process is termed the “depletion layer”. When the depletion layer is formed, the electron transfer from the solid electrode to the electrolyte in the solution phase becomes difficult due to the lack of electrons near the solid electrode surface.

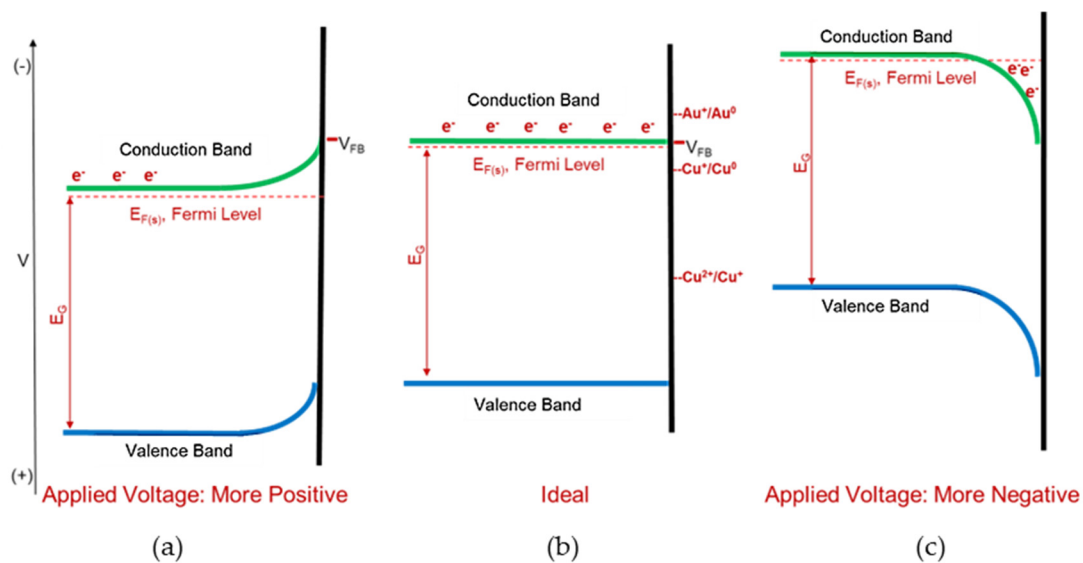


**Figure 19.** Schematic diagram of energy bands of n-type semiconductors upon (a) applying more positive potential, (b) applying ideal potential, and (c) applying more negative potential.

Figure 19c shows the energy band diagram when a negative potential is applied to the semiconductor electrode. When the applied potential is more negative than the flat band potential, the Fermi level shifts up, and the  $E_v$  and  $E_c$  bend like the figure; i.e., the energy level is higher at the solid bulk phase and lower at the surface. In this case, electrons in the conduction band move to the surface (lower energy level) from the bulk phase (higher energy level), and an “electron-rich” surface layer termed the “space charge layer” is formed near the surface [25]. Because of the presence of electrons near the surface, electron transfer from the solid electrode to the electrolyte in the solution phase becomes more accessible. Thus, a reduction of electrolytes can occur.

In most cases, the electrolyte’s electron transfer rate or reduction rate is proportional to the number density of the surface electrons at the energy level and is the same as the reduction potential of the electrolyte (oxidized chemical species). If the reduction potential is positioned in the range between the  $E_c$  at the surface and the  $E_f$ , the number density of electrons is high, and a rapid reduction proceeds [23]. Suppose the reduction potential is out of the range. In that case, however, there is no electron at the same energy level as the reduction potential of the electrolyte, and reduction of the electrolyte does not occur (or the reduction rate is prolonged).

Figure 20 compares the energy band diagrams for two iron oxides (magnetite and hematite) and rutile when applying negative electrode potential. In the case of rutile (Figure 20c), the positions of the reduction potential for the electrolytes, such as  $\text{Au}^+$ ,  $\text{Cu}^+$ , and  $\text{Cu}^{2+}$ , are higher than that of the  $E_c$  at the surface. Because of this relative position, a rapid electron transfer from rutile to these species may be possible when the applied electrode potential is low enough and the corresponding Fermi level is higher than the reduction potential. On the other hand, in the case of iron oxides (Figure 20a,b), the position of the reduction potential for  $\text{Au}^+$  is higher than the  $E_c$  for magnetite or near the  $E_c$  for hematite, while the  $\text{Cu}^+$  and  $\text{Cu}^{2+}$  positions are inside the band gap and below the  $E_c$ . This result means reducing  $\text{Au}^+$  is possible, but reducing  $\text{Cu}^{2+}$  and  $\text{Cu}^+$  is difficult. This configuration may be the reason iron oxides selectively cement gold.

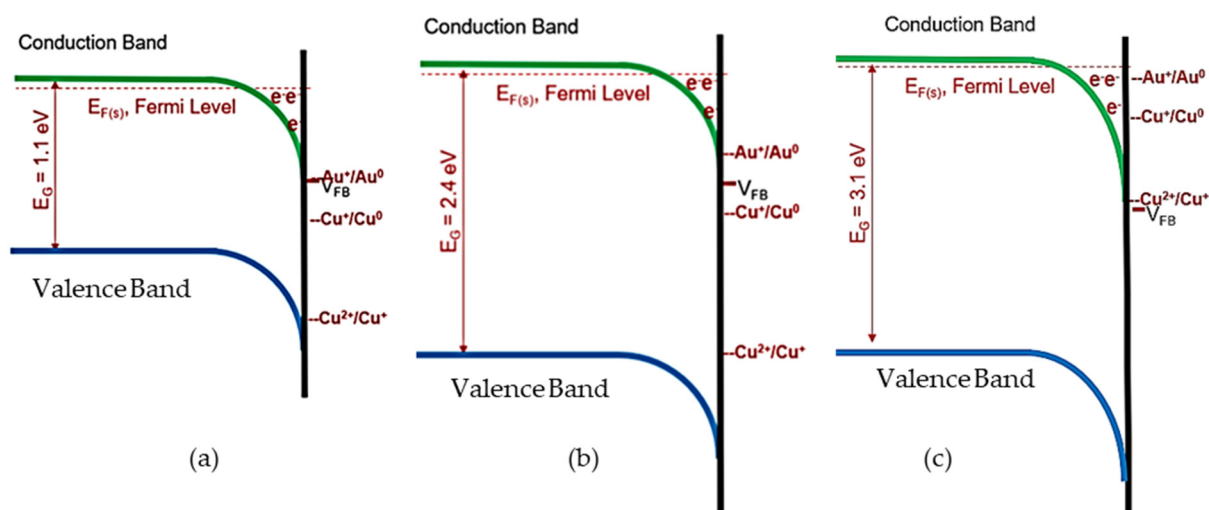


**Figure 20.** Energy band diagrams after negative electrode potential is applied for (a) magnetite, (b) hematite, and (c) rutile.

The proposed selective mechanism of iron oxide to gold is presented in Figure 21. The proposed mechanism is supported by various electrochemical, spectrophotometric, and surface analysis results in Figures 3–17. The electron transfer mechanism across the  $\text{Al}_2\text{O}_3$  layer between the ZVAI and iron oxide particles was discussed in previous research [1], where the ZVAI surface might be covered with a fragile layer of  $\text{Al}_2\text{O}_3$ . Since  $\text{Al}_2\text{O}_3$  is an electric insulating material, direct current cannot pass through this layer. Interpretation for the electron transfer through the insulating  $\text{Al}_2\text{O}_3$  layer is via (1) the quantum tunneling effect [21] and (2) alternative current transfer through the  $\text{Al}_2\text{O}_3$  layer acting as a capacitor [16]. From then on, electrons that pass through the solid–electrolyte interface can be interpreted using the energy band diagram. With staircase potential electrochemical impedance spectroscopy, the iron oxides confirm that the flat band potential of magnetite and hematite is around  $-0.9$  V and  $-1.0$  V, respectively. These results further confirm that by linear interpolation on the positive slope in the M-S plot, both iron oxides used in these experiments are n-type semiconductors, as presented in Figure 16.

The Fermi level and flat band potential of the n-type semiconductor sit just below the conduction band edge. Initially, this edge has no depletion layer (empty) at the junction between the electrolyte and the semiconductor. Then, electrons will flow from the semiconductor to the electrolyte interface, filling the depletion layer with electrons. This transfer of electrons bends and creates a layer near the semiconductor surface called the space charge layer. The extent of bending using iron oxides will only create a space charge layer across the  $\text{Au}(\text{S}_2\text{O}_3)_2^{3-}$  reduction band edge around  $-1.0$  V since the flat band potentials of magnetite and hematite are around  $-0.9$  V and  $-1.0$  V, respectively. Copper ions will not be able to accept electrons from the semiconductor interface since the electrolytes' reduction potentials are around  $-0.8$  V for  $\text{Cu}^+/\text{Cu}^0$  and  $-0.2$  V for  $\text{Cu}^{2+}/\text{Cu}^+$ , respectively. The proposed phenomenon suggests that by configuring the relative energy band diagrams of hematite and magnetite, their semiconductive properties facilitate the travel of electrons from the iron oxide–electrolyte interface, thereby enabling selective cementation towards  $\text{Au}(\text{S}_2\text{O}_3)_2^{3-}$  ions in gold–copper ammoniacal thiosulfate solutions.

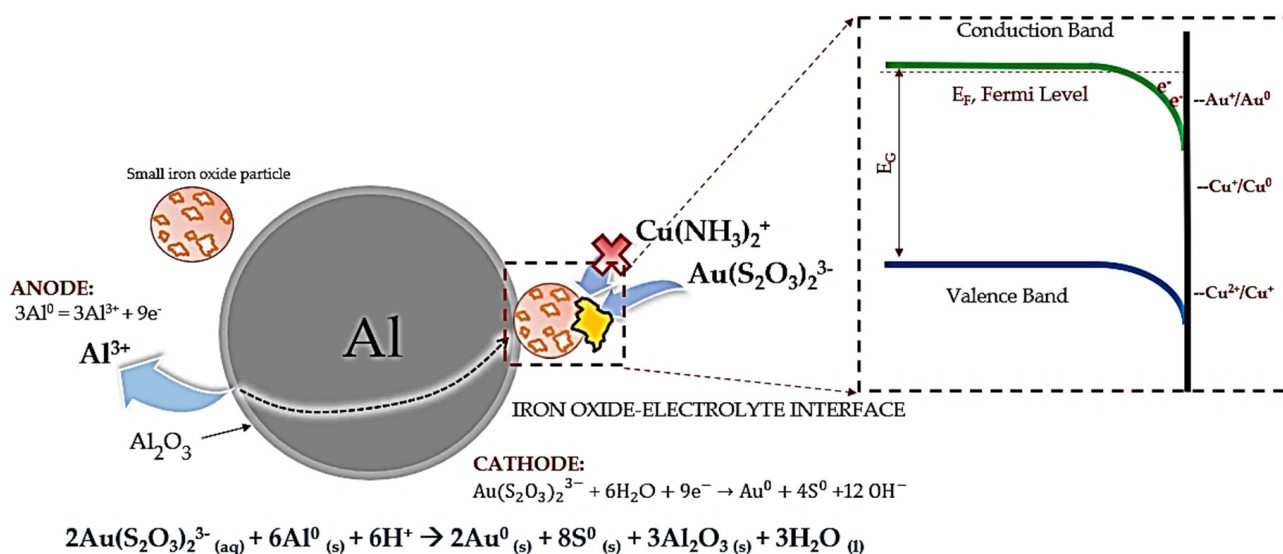


**Figure 21.** Schematic diagram of iron oxide's selective cementation mechanism to gold as an electron mediator upon galvanic interaction with zero-valent aluminum.

#### 4. Conclusions

Cementation experiments were conducted using various metal oxides, including magnetite, hematite, and titanium oxides (anatase and rutile) as electron mediators to investigate the direct influence of semiconductive properties on the galvanic interaction with zero-valent aluminum as an electron donor upon the cementation process. The results in Figures 2–4 further validate that using iron oxides has shown better selectivity for gold during cementation than titanium. The latter investigated the semiconductive properties of metal oxides, such as the energy band gap and the flat band potential, to estimate the configuration of the energy band diagram.

By configuring the energy band diagrams supported by various electrochemical experiments presented in Figures 16–21, it was found that the bending occurs from the flat band potential edge to the conducting band edge; in both cases, magnetite and hematite have a flat band potential near the conduction band edge where electrons can transfer from the semiconductive electrode interface across the electrolyte interface (reduction band edge) of gold around  $-1.0$  V only. This research concludes that the representation of energy band diagrams was able to explain why iron oxides are selective only for gold upon the cementation process in gold–copper ammoniacal thiosulfate media and that the semiconductive property governs the said selective cementation.

**Author Contributions:** Conceptualization, J.Z., I.P., M.I. and N.H.; methodology, J.Z. and N.H.; validation, N.O. and Y.E.; software, N.O. and Y.E.; investigation, J.Z., K.A., N.O. and Y.E.; analysis, N.O. and Y.E.; writing—original draft preparation, J.Z. and K.A.; writing—review and editing, J.Z., K.A., I.P., M.I., Y.E. and N.H. All authors have read and agreed to the published version of the manuscript.

**Funding:** This research received no external funding.

**Data Availability Statement:** The raw data supporting the conclusions of this article will be made available by the authors on request.

**Conflicts of Interest:** The authors declare no conflict of interest.

## References

1. Zoleta, J.; Jeon, S.; Kuze, A.; Okada, N.; Park, I.; Ito, M.; Elakneswaran, Y.; Hiroyoshi, N. Selective Cementation of Gold Using an Iron Oxide and Zero-Valent Aluminum Galvanic System from Gold–Copper Ammoniacal Thiosulfate Solutions. *Metals* **2023**, *13*, 1289. [[CrossRef](#)]
2. Qin, H.; Guo, X.; Tian, Q.; Zhang, L. Pyrite enhanced chlorination roasting and its efficacy in gold and silver recovery from gold tailing. *Sep. Purif. Technol.* **2020**, *250*, 117168. [[CrossRef](#)]
3. Qin, H.; Guo, X.; Tian, Q.; Yu, D.; Zhang, L. Recovery of Gold from sulfide refractory gold ore: Oxidation roasting pretreatment and gold extraction. *Miner. Eng.* **2021**, *164*, 106822. [[CrossRef](#)]
4. Konadu, K.T.; Huddy, R.J.; Harrison, S.T.; Osseo-Asare, K.; Sasaki, K. Sequential pretreatment of double refractory gold ore (DRGO) with a thermophilic iron oxidizing archaeon and fungal crude enzymes. *Miner. Eng.* **2019**, *138*, 86–94. [[CrossRef](#)]
5. Nan, X.-Y.; Cai, X.; Jun, K. Pretreatment Process on Refractory Gold Ores with As. *ISIJ Int.* **2014**, *54*, 543–547. [[CrossRef](#)]
6. Xie, F.; Chen, J.-N.; Wang, J.; Wang, W. Review of gold leaching in thiosulfate-based solutions. *Trans. Nonferrous Met. Soc. China* **2021**, *31*, 3506–3529. [[CrossRef](#)]
7. Qin, H.; Guo, X.-Y.; Tian, Q.-H.; Zhang, L. Recovery of gold from refractory gold ores: Effect of pyrite on the stability of the thiourea leaching system. *Int. J. Miner. Met. Mater.* **2021**, *28*, 956–964. [[CrossRef](#)]
8. Sun, C.-B.; Zhang, X.-L.; Kou, J.; Xing, Y. A review of gold extraction using noncyanide lixiviants: Fundamentals, advancements, and challenges toward alkaline sulfur-containing leaching agents. *Int. J. Miner. Met. Mater.* **2020**, *27*, 417–431. [[CrossRef](#)]
9. Tremblay, L.; Deschênes, G.; Ghali, E.; McMullen, J.; Lanouette, M. Gold recovery from a sulphide bearing gold ore by percolation leaching with thiourea. *Int. J. Miner. Process.* **1996**, *48*, 225. [[CrossRef](#)]
10. Ma, C.J.; Li, J.Y.; Liu, R.J. A review of thiocyanate hydrometallurgy for the recovery of gold. *Appl. Mech. Mater.* **2015**, *768*, 53. [[CrossRef](#)]
11. Ahtiainen, R.; Lundström, M. Cyanide-free gold leaching in exceptionally mild chloride solutions. *J. Cleaner Prod.* **2019**, *234*, 9. [[CrossRef](#)]
12. Ahtiainen, R.; Lundström, M.; Liipo, J. Preg-robbing verification and prevention in gold chloride-bromide leaching. *Miner. Eng.* **2018**, *128*, 153. [[CrossRef](#)]
13. Wang, H.-X.; Sun, C.-B.; Li, S.-Y.; Fu, P.-F.; Song, Y.-G.; Li, L.; Xie, W.-Q. Study on gold concentrate leaching by iodine-iodide. *Int. J. Miner. Met. Mater.* **2013**, *20*, 323–328. [[CrossRef](#)]
14. Konyratbekova, S.; Baikonurova, A.; Ussoltseva, G.; Erust, C.; Akcil, A. Thermodynamic and kinetic of iodine-iodide leaching in gold hydrometallurgy. *Trans. Nonferrous Met. Soc. China* **2015**, *25*, 3774. [[CrossRef](#)]
15. Jeon, S.; Tabelin, C.B.; Takahashi, H.; Park, I.; Ito, M.; Hiroyoshi, N. Enhanced Cementation of gold via galvanic interaction using activated carbon and zero-valent aluminum: A novel approach to recover gold ions from ammonium thiosulfate medium. *Hydrometallurgy* **2020**, *191*, 105165. [[CrossRef](#)]
16. Zoleta, J.B.; Itao, G.B.; Resabal VJ, T.; Lubguban, A.A.; Corpuz, R.D.; Ito, M.; Tabelin, C.B. Improved pyrolysis behavior of ammonium polyphosphate-melamine-expandable (APP-MEL-EG) intumescent fire-retardant coating system using ceria and dolomite as additives for I-beam steel application. *Heliyon* **2020**, *6*, e03119. [[CrossRef](#)] [[PubMed](#)]
17. Zoleta, J.; Itao, G.; Resabal, V.J.; Lubguban, A.; Corpuz, R.; Tabelin, C.; Hiroyoshi, N. CeO<sub>2</sub>-Dolomite as fire retardant additives on the conventional intumescent coating in steel substrate for improved performance. *MATEC Web Conf.* **2019**, *268*, 04009. [[CrossRef](#)]
18. Tabelin, C.B.; Veerawattananun, S.; Ito, M.; Hiroyoshi, N.; Igarashi, T. Pyrite oxidation in the presence of hematite and alumina: II. Effects on the cathodic and anodic half-cell reactions. *Sci. Total Environ.* **2017**, *581–582*, 126–135. [[CrossRef](#)] [[PubMed](#)]
19. Ke, B.; Li, Y.; Chen, J.; Zhao, C.; Chen, Y. DFT study on the galvanic interaction between pyrite (100) and galena (100) surfaces. *Appl. Surf. Sci.* **2016**, *367*, 270–276. [[CrossRef](#)]
20. Gelderman, K.; Lee, L.; Donne, S.W. Flat-band potential of a semiconductor: Using the mott–schottky equation. *J. Chem. Educ.* **2007**, *84*, 685. [[CrossRef](#)]
21. Kennedy, J.H.; Shinar, R.; Ziegler, J.P.  $\alpha$ -Fe<sub>2</sub>O<sub>3</sub> Photoanodes Doped with Silicon. *J. Electrochem. Soc.* **1980**, *127*, 2307. [[CrossRef](#)]
22. Alberty, W.J.; O’Shea, G.J.; Smith, A.L. Interpretation and use of mott–schottky plots at the semiconductor/electrolyte interface. *J. Chem. Soc. Faraday Trans.* **1996**, *92*, 4083–4085. [[CrossRef](#)]
23. Hankin, A.; Bedoya-Lora, F.E.; Alexander, J.C.; Regoutz, A.; Kelsall, G.H. Flat band potential determination: Avoiding the pitfalls. *J. Mater. Chem. A* **2019**, *7*, 26162–26176. [[CrossRef](#)]
24. Radecka, M.; Rekas, M.; Trenczek-Zajac, A.; Zakrzewska, K. Importance of the band gap energy and flat band potential for application of modified tio<sub>2</sub> photoanodes in water photolysis. *J. Power Sources* **2008**, *181*, 46–55. [[CrossRef](#)]
25. Makula, P.; Pacia, M.; Macyk, W. How to Correctly Determine the Band Gap Energy of Modified Semiconductor Photocatalysts Based on UV–Vis Spectra. *J. Phys. Chem. Lett.* **2018**, *9*, 6814–6817. [[CrossRef](#)] [[PubMed](#)]
26. Ionel, Ş.; Alexandru, E. Metal Oxides-Based Semiconductors for Biosensors Applications. *Front. Chem. J.* **2020**, *8*, 2296–2646. [[CrossRef](#)]
27. Balasubramani, V.; Chandraleka, S.; Rao, T.S.; Sasikumar, R.; Kuppasamy, M.R.; Sridhar, T.M. Review-Recent Advances in Electrochemical Impedance Spectroscopy Based Toxic Gas Sensors Using semiconducting metal oxides. *J. Electrochem. Soc.* **2020**, *167*, 037572. [[CrossRef](#)]
28. Patil, S.A.; Shinde, D.V.; Kim, E.K.; Lee, J.K.; Mane, R.S.; Han, S.H. Photoelectrochemistry of solution processed hematite nanoparticles, nanoparticle-chains and nanorods. *RSC Adv.* **2012**, *2*, 11808–11812. [[CrossRef](#)]

29. Bredar, A.R.; Chown, A.L.; Burton, A.R.; Farnum, B.H. Electrochemical Impedance Spectroscopy of Metal Oxide Electrodes for Energy Applications. *ACS Appl. Energy Mater.* **2020**, *3*, 66–98. [[CrossRef](#)]
30. Van de Krol, R.; Grätzel, M. *Photoelectrochemical Hydrogen Production*; Springer: New York, NY, USA, 2012; ISBN 978-1-4614-1379-0. [[CrossRef](#)]

**Disclaimer/Publisher’s Note:** The statements, opinions and data contained in all publications are solely those of the individual author(s) and contributor(s) and not of MDPI and/or the editor(s). MDPI and/or the editor(s) disclaim responsibility for any injury to people or property resulting from any ideas, methods, instructions or products referred to in the content.